Global and Planetary Change 190 (2020) 103155

Contents lists available at ScienceDirect

Global and Planetary Change

journal homepage: www.elsevier.com/locate/gloplacha

Research article

Large environmental disturbances caused by magmatic activity during the Late Devonian Hangenberg Crisis

Agnieszka Pisarzowska[a,*], Michał Rakociński[a], Leszek Marynowski[a], Marek Szczerba[b], Marie Thoby[c], Mariusz Paszkowski[b], Maria Cristina Perri[d], Claudia Spalletta[d], Hans-Peter Schönlaub[e], Nina Kowalik[b], Manfred Gereke[f]

[a] Institute of Earth Sciences, University of Silesia in Katowice, Będzińska 60, 41-200 Sosnowiec, Poland
[b] Institute of Geological Sciences, Polish Academy of Sciences – Research Centre in Kraków, Senacka 1, 31-002 Kraków, Poland
[c] Laboratoire Géosciences Océan (LGO), CNRS-UMR6538, Université Bretagne Occidentale, Brest, France
[d] Dipartimento di Scienze Biologiche, Geologiche e Ambientali, Alma Mater-Università di Bologna, via Zamboni 67, 40126 Bologna, Italy
[e] Austrian Academy of Sciences, Commission for Geosciences, Dr. Ignaz Seipel-Platz 2, A-1010 Vienna, Austria
[f] Hopfengarten 6, 35038 Heskem-Mölln, Germany

ARTICLE INFO

Keywords:
Carbon and molybdenum isotopes
Volcanic activity
Inorganic geochemistry
Mineralogical composition
Redox conditions
Hangenberg Black Shale

ABSTRACT

A wide range of various proxies (e.g., mineralogy, organic carbon, inorganic geochemistry, C and Mo isotopes, and framboidal pyrite) were applied for interpretation of changing oceanic redox conditions, bioproductivity, and the regional history of magmatic activity. This resulted in internally consistent interpretation of the late Famennian Hangenberg Crisis in subtropical deepest water sites of the epeiric Rhenohercynian and Saxo–Thuringian basins, as well as more open sites of the Paleo-Tethys Ocean.

High mercury concentrations were detected in all of the studied sections, with the highest values strata in the Carnic Alps (up to 20 ppm) and Thuringia (up to 1.5 ppm). The beginning of the Hg anomaly and the presence of pyroclastic material, indicate that local magmatic activity was initiated before the deposition of the Hangenberg Black Shale (HBS). The onset of the HBS deposition coincided with the expansion of phosphate-enriched, anoxic to euxinic waters during short-lived CO_2-greenhouse spike of a warm–humid climate. Intensive magmatic activity was a trigger for climatic changes, an excessive eutrophication, and an accelerated burial of organic carbon during the Hangenberg transgressive pulse. The injection of catastrophic amounts of CO_2, toxic elements and acids from volcanic activity could have led to acidification, mutation of spores, and episodes of mass mortality of marine plankton.

1. Introduction

The end-Devonian Hangenberg Crisis (HBC; i.e., the Hangenberg Event) represents one of the most crucial periods in the evolution of the biosphere. This event began with the deposition of a transgressive organic-rich shale (Hangenberg Black Shale, HBS; Fig. 1), and then regressive units of grey shale (Hangenberg Shale, HS), sandstone (Hangenberg Sandstone, HSS), and limestone (Stockum Limestone, SL) (Caplan and Bustin, 1999; Kaiser et al., 2015). Based on German lithological marker units, the Hangenberg Event has been subdivided into clearly defined lower, middle and upper parts. The event had a worldwide effect and is well documented, although there is no clear consensus on the forcing mechanism(s). Glacioeustatic changes, climate fluctuations, volcanism, asteroid impacts, phytoplankton blooms, and the spread of terrestrial plants have all been proposed as possible causes and triggers (e.g., Caplan and Bustin, 1999; Streel et al., 2000; Kaiser et al., 2006; Marynowski et al., 2012; Carmichael et al., 2016; Paschall et al., 2019).

Linkages between anoxia, transgression, and warming have been suggested for the Late Devonian oceanic anoxic event horizons (e.g., Sandberg et al., 2002; De Vleeschouwer et al., 2013). Strata recording anoxic/dysoxic and/or euxinic conditions across the Famennian–Tournaisian interval are well-documented in low paleolatitudinal regions of Europe, North Africa, the United States, Canada, Russia, Thailand, southern China, and northeastern Vietnam (e.g., Komatsu et al., 2014; Kumpan et al., 2015; Matyja et al., 2015; Qie et al., 2015; Carmichael et al., 2016; Kalvoda et al., 2018; Martinez et al., 2019; Paschall et al., 2019). The deposition of black shale has

* Corresponding author.
E-mail address: agnieszka.pisarzowska@us.edu.pl (A. Pisarzowska).

https://doi.org/10.1016/j.gloplacha.2020.103155
Received 2 July 2019; Received in revised form 21 February 2020; Accepted 29 February 2020
Available online 05 March 2020

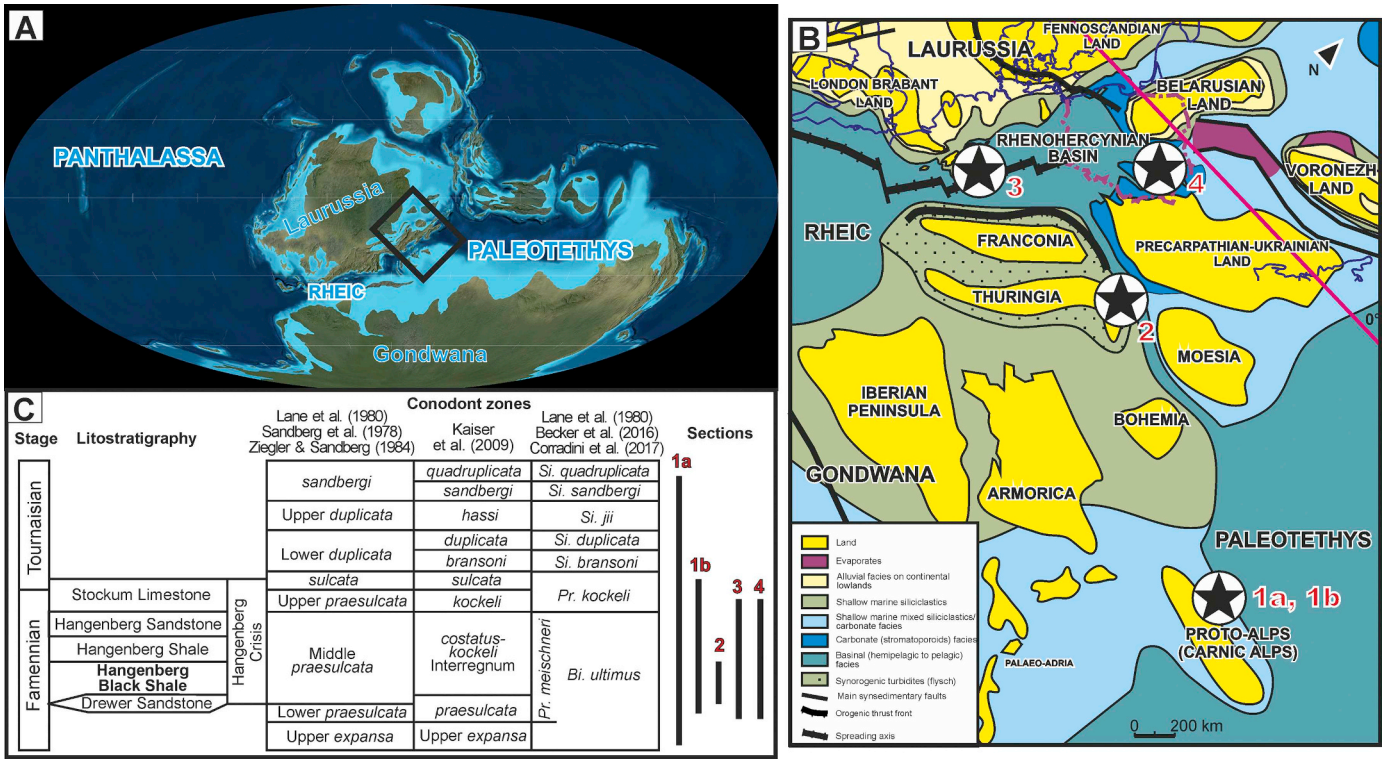

Fig. 1. (A) Late Devonian (360 Ma) paleogeography after Blakey (2016). (B) Location of the studied sections: (1a) Plan di Zermula A (Carnic Alps), (1b) Kronhofgraben (Carnic Alps), (2) Kahlleite (Thuringia), (3) Drewer (Rhenish Massif), (4) Kowala (Holy Cross Mountains). Palaeogeographic reconstruction after Paproth (1986) and Franke et al. (2017), modified. (C) Biostratigraphy, lithostratigraphy and event-stratigraphy of the Devonian-Carboniferous boundary interval and biostratigraphic range of the investigated sections. The Hangenberg Crisis with lithostratigraphic units from the type area in the Rhenish Massif (after Becker et al., 2016 and Kaiser et al., 2015). Abbreviations: *Bi.* - *Bispathodus*, Pr. – *Protognathodus*, Si. – *Siphonodella*.

been commonly interpreted as a consequence of increased nutrient fluxes that accompanied accelerated continental weathering (Wilder, 1994; Algeo and Scheckler, 1998; Percival et al., 2019) or upwelling of deeper waters (e.g. Caplan et al., 1996).

Subaerial and/or submarine multiple eruptions of enormous magmatic flows may alter the ocean–atmosphere system by introducing gases and elements, which are potentially conducive to either a warmer or cooler climate, and can potentially significantly change the structure and chemistry of the oceans (Erba et al., 2015; Jones et al., 2016; Racki, 2020b). Large igneous provinces (LIPs) have been suggested as a significant extinction driver for the Frasnian–Famennian (Racki et al., 2018b; Racki, 2020a), Permian–Triassic (Courtillot and Renne, 2003), Triassic–Jurassic (Percival et al., 2017), and other mass extinctions (Wignall, 2005; Ernst, 2014; Racki, 2020b). Recently, a growing number of publications have highlighted the potential impact of volcanism during the HBC (Marynowski et al., 2012; Kalvoda et al., 2019; Paschall et al., 2019).

Changes in primary productivity, anoxia, and volcanic degassing are reflected in carbon isotope records. Molybdenum isotopes can yield information regarding the average global-ocean redox conditions in paleo-marine systems (Siebert et al., 2003; Arnold et al., 2004; Scott and Lyons, 2012). The carbon isotope record in carbonates ($\delta^{13}C_{carb}$) related to the Hangenberg Crisis has been reported by numerous authors (e.g., Buggisch and Joachimski, 2006; Kaiser et al., 2006; Kumpan et al., 2014a, 2014b). Comparison of global carbon isotope records show a high variability during the late Famennian–early Tournaisian (Table 1), on both regional and local scales (Carmichael et al., 2016).

Recent, high-resolution chemostratigraphic studies of carbonate and organic C isotopes have suggested a more complex pattern, whereby negative excursions exist in Middle *praesulcata* conodont Zone and Devonian–Carboniferous boundary, and are followed by a positive shift in the lower part of the Upper *praesulcata* Zone (Kaiser et al., 2008; Qie et al., 2015). Compared with the carbon cycle, a relatively small amount of research has been undertaken, to date, regarding the marine Mo cycle during the Hangenberg Event (Dahl et al., 2010; Yang, 2019). In order to better understand the environmental and biological conditions associated with the biotic extinction during the HBC, we present new isotopic data from the Rhenish Massif, Thuringia, Carnic Alps, and the Holy Cross Mountains situated in the Rhenohercynian and Saxo–Thuringian basins and part of the Paleo-Tethys Ocean (Fig. 1). High-resolution C and Mo isotopic records, supported by mineralogical and geochemical data, provide insight into the water-column redox structure of these basins, nutrient cycling, and volcanic activity, especially during the early crisis interval that concerned the main marine extinction and increased carbon burial event.

2. Regional setting

2.1. Carnic Alps

The Kronhofgraben section, Austria (N46°36'00.0", E13°02'02.0") and Plan di Zermula A section, Italy (N46°34'31.0", E13°06'41.0") are located in the central part of the Carnic Alps. The Kronhofgraben section is situated in a gorge of the Aßnitzbach River, ca. 7 km on the east of Plöckenpass, and ca. 1 km northwest of Kronhof Törl pass at the Austrian–Italian border. The Plan di Zermula A section appears on the western slope of Mount Zermula massif, along the road from Paularo to Stua di Ramaz. Grey limestone and black shale of the Pal Grande Formation (Spalletta et al., 2015; Spalletta et al., 2020) make up the studied interval in both sections. The black shale was interpreted as an HBS equivalent, and the HBS horizon was assigned to the Middle *praesulcata* Zone in Kronhofgraben (40-cm-thick) and Plan di Zermula A (15-cm-thick), by Kaiser (2005). The HBS is underlain by cephalopod-bearing limestone of the Upper *expansa*–Lower *praesulcata* Zone. Perri

Table 1
Compilation of data documented carbon isotope anomaly for the Hangenberg Crisis.

Locality	Carbon isotope anomaly	Reference
Carnic Alps (Grüne Schneid)	Positive ($\delta^{13}C_{carb}$)	Kaiser et al. (2006)
Graz (Trolp)	Positive ($\delta^{13}C_{carb}$)	Kaiser et al. (2008)
Austria (Steinberg)	Negative ($\delta^{13}C_{carb}$)	Bojar et al. (2013)
Moravian Karst	Positive ($\delta^{13}C_{carb}$) (Lesní lom Quarry); negative ($\delta^{13}C_{carb}$) (Křtiny)	Kumpan et al. (2014a)
Rhenish Massif (Drewer)	Lack of $\delta^{13}C_{carb}$ anomaly	Buggisch and Joachimski (2006)
Namur-Dinant Basin	Negative to positive ($\delta^{13}C_{carb}$) (Gendron-Celles), positive ($\delta^{13}C_{carb}$) (Anseremme)	Buggisch and Joachimski (2006), Kumpan et al. (2014b)
Montagne Noire, France (La Serre trench E')	Positive ($\delta^{13}C_{carb}$ in brachiopod shells and ooids); negative ($\delta^{13}C_{carb}$ in matrix)	Brand et al. (2004), Buggisch and Joachimski (2006)
Pyrenees, France (Milles)	Lack of $\delta^{13}C_{carb}$ anomaly	Kaiser (2005)
Pechora Plate, Russia	Lack of $\delta^{13}C_{carb}$ anomaly; negative $\delta^{13}C$ anomaly in conodont organic matter	Zhuravlev and Sobolev (2019)
South China	Lack of $\delta^{13}C_{carb}$ anomaly (Malanbian, Qilinzhai); negative ($\delta^{13}C_{carb}$) (Long'an)	Qie et al. (2015)
Vietnam	Lack of $\delta^{13}C_{carb}$ anomaly; positive ($\delta^{13}C_{org}$) anomaly	Paschall et al. (2019), Shizuya et al. (2020)
Thailand	Positive ($\delta^{13}C_{carb}$)	Königshof et al. (2012)
North America	Positive ($\delta^{13}C_{carb}$) (western Illinois basin and Chaffee Group of Colorado); negative ($\delta^{13}C_{carb}$) (Chaffee Group of Colorado); negative to positive ($\delta^{13}C_{carb}$) (Missouri), positive and lack of $\delta^{13}C_{org}$ anomaly (Appalachian Basin)	Cramer et al. (2008), Day et al. (2013), Myrow et al. (2013), Martinez et al. (2019)

and Spalletta (2001) indicated for the HBS horizon at Plan di Zermula A section a time span corresponding to the interval Middle–Upper *praesulcata* zones. In both sections the missing interval corresponds to this interval (Spalletta et al., 2020). The first carbonate bed above the HBS belongs to the *sulcata* Zone (Perri and Spalletta, 2001; Kaiser et al., 2009). In a re-study of the Kronhofgraben and Plan di Zermula A sections, Spalletta et al. (2020) correlated the HBS horizon with the upper part of the *Protognathodus meischneri* subzone, equating with the Lower *praesulcata* Zone. The underlain limestone units were correlated with the lower part of the same subzone, and the overlying limestone with the upper part of the *Protognathodus kockeli* Zone. These stratigraphic revisions resulted from application of the new conodont zonations proposed by Corradini et al. (2017) and Spalletta et al. (2017).

The D–C boundary successions in the two sections were deposited in a deep water environment within the tropical belt, around 30° S or less latitude (Fig. 1; Schönlaub et al., 1992; Schönlaub, 2018). During the Late Devonian, the Carnic Alps were the northern tips of the African part of Eastern Gondwana (Schönlaub and Histon, 2000) and belonged to the Gondwana-derived Noric Terrane (Frisch and Neubauer, 1989; part of Palaeo-Adria microcontinent by Franke et al., 2017). The Variscan orogeny in this area more likely was the result of a transpressive event (Spalletta and Venturini, 1995), which fits very well with the absence of an ocean between the south eastern part of Laurussia and Gondwana (Franke et al., 2017). The eruption of submarine, alkali basalts on the Austrian (Raabtal volcanism) and Italian (Dimon Formation, Venturini and Spalletta, 2015) sides occurred during the early Carboniferous (see Pasquarè Mariotto and Venturini, 2019).

2.2. Rhenish Massif

The uppermost Famennian samples were collected from the Drewer section, located in the northern part of the Rhenish Massif (Germany). Drewer (N51°29.616′; E8°21.360′) is the an abandoned quarry located on the Belecke anticline (Klein, 2016; Becker et al., 2016) north of Warstein, ~62 km east of the center of Dortmund. The samples were collected from the WA Section (Drewer I) (see Korn, 1991). The uppermost Famennian stage in the studied sections consists of alternating shale and nodular limestone (Wocklum Limestone) of the Upper *expansa* Zone. The Drewer Sandstone is intercalated in the Wocklum Limestone in its upper part. The Wocklum Limestone is followed by the HBS (*costatus-kockeli* Interregnum; Van Steenwinkel, 1993) and overlying siliciclastic successions (the Hangenberg Sandstone in the Drewer section) of the upper part of the *costatus–kockeli* Interregnum.

During the Late Devonian, the studied region of the Rhenish Massif was a shelf area of a Rhenohercynian Ocean situated on the southern margins of Laurussia (Fig. 1), where sedimentation was controlled by sea level fluctuations, syn-sedimentary tectonic activity, and variations in the input of siliciclastic material derived mainly from Baltica (Franke et al., 1978; Paproth, 1986; Königshof et al., 2016; Kołtonik et al., 2018, 2019). The well-exposed HBS has been interpreted to be a transgressive system tract associated with low sedimentation rates (Van Steenwinkel, 1984), whereas the HBS has been interpreted as a high-stand system tract deposit, and the HSS a basin-floor fan deposit (Kaiser et al., 2015).

2.3. Thuringia

The Kahlleite section (50°37'32.5" N; 11°50'32.2" E) is within an inactive quarry, 1 km southwest of Rödersdorf near Gera, which is situated on the northwest flank of the Berga anticline (Gereke, 2004, 2007). Thuringia (with Franconia) belonged to the Gondwana-derived North Armorica microcontinent, located between Laurussia and Gondwana (Fig. 1). Until the Devonian, the Saxo–Thuringian Ocean separated North and South Armorica (Franke et al., 2017).

2.4. Holy Cross Mountains

The Kowala section is situated in the northeastern wall of the large, active quarry located on the southern limb of the Gałęzice–Kowala syncline. This area belongs to a distinct paleogeographic and tectonic region of the Holy Cross area: Chęciny-Zbrza basin in the Kielce paleohigh (i.e., northern part of the Małopolska Block; e.g., Racki et al., 2002). The investigated interval (ca. 2.3-m-thick) belongs to the upper part of lithological set L (*sensu* Berkowski, 2002), and M (*sensu* De Vleeschouwer et al., 2013), which are equivalent to sets B and C (*sensu* Malec, 2014) in the trench. The section below the black shale, which was interpreted as an HBS equivalent, consists of green and cherry red, nodular, marly limestone, with abundant cephalopods (= *Wocklumeria* Limestones), and marly shale with several thin tuffite layers (Marynowski and Filipiak, 2007). The HBS is overlain by green and brown claystone, tuffite, and marly shale. The sampled succession is assigned to the *praesulcata* conodont Zone and to the LN miospore Zone (Olempska, 1997; Marynowski and Filipiak, 2007; Filipiak and Racki, 2010). During the Late Devonian to Early Carboniferous, this area was an easternmost part of the Rhenohercynian Ocean, located on the southern margins of Laurussia (Fig. 1; Ziegler, 1990).

3. Methodology

3.1. XRD

The mineralogy of samples was determined on randomly oriented powder specimens with XRD analysis at the Institute of Geological

Sciences, Polish Academy of Sciences (IGS PAS, Kraków, Poland), using a Thermo ARL X'tra diffractometer. Ten percent of an internal ZnO standard was added to samples and then milled in a McCrone micronizing mill for 5 min. Diffractograms were recorded in the range of 5–65° 2Θ with a step of 0.02° (5 s/step). Q-Min software (M. Szczerba, unpublished) was used for quantitative analysis. Mineralogical analyses were then coupled with chemical data of major elements using approach described by McCarty et al. (2015). The aim was to obtain information about chemical composition of minerals with variable formulas (e.g. phyllosilicates, ankerite, feldspars). Additional details concerning XRD analysis of clay-minerals are presented in Supplementary Data 1.

3.2. Total organic carbon (TOC) determination

Percent concentrations of carbon were determined using a Vario MicroCUBE elemental analyzer at the IGS PAS (Warsaw, Poland). Samples wrapped in tin capsules were combusted at 1150 °C. The released gas was separated on a GC column and measured using a thermal conductivity detector. Values were normalized to a sulphanilic acid standard. The results of this measurement are reported in wt% and have a precision of better than ± 0.18%.

3.3. Inorganic geochemistry

Fifty-five samples were ground in an agate mill and analyzed for the majority of elements at the Bureau Veritas Mineral Laboratories in Perth, Australia (Kronhofgraben, Plan di Zermula A) and in Ancaster, Ontario, Canada (Drewer, Kahlleite and Kowala). Analytical details are presented in Supplementary Data 1.

Enrichment factors (EF) were calculated as: $X_{EF} = [(X/Al_{sample}/(X/Al)_{PAAS}]$ for shale and siltstone and as $X_{EF} = [(X/Al_{sample}/(X/Al)_{WED}]$ for carbonate; where X and Al represent the weight percent concentrations of elements X and Al, respectively. Samples were normalized using the post-Archean Australian average shale (PAAS) compositions of Taylor and McLennan (1985; see also Tribovillard et al., 2012) for shale and siltstone, as well as the average limestone (WED; Wedepohl, 1970) for carbonate. Any relative enrichment was then expressed by an EF > 1, a depletion by an EF < 1.

3.4. Stable isotopes

3.4.1. Carbon isotopes

Samples for carbon isotope analyses were powdered and acidified with an excess of 10% HCl and were kept at 60 °C for at least 8 h to remove inorganic carbonate material. Samples were then rinsed with ultrapure (> 18 MΩ) deionized water to remove acid and were oven-dried at 60 °C. Analyses of sedimentary organic carbon ($\delta^{13}C_{org}$) isotope signatures were carried out using a Thermo Flash EA 1112HT elemental analyser connected to a Thermo Delta V Advantage isotope ratio mass spectrometer in a Continuous Flow system at IGS PAS (Warsaw). Isotopic values for carbon are reported in per mil (‰) relative to the Vienna PeeDee Belemnite (VPDB) standard and calibrated using certified international standards. The precision of $\delta^{13}C$ analyses is ± 0.33‰.

Powdered samples for $\delta^{13}C$ analyses in carbonate were reacted with 100% H_3PO_4 at 70 °C to produce CO_2. Isotope measurements were conducted with a KIEL IV Device that was connected on-line to a FinniganMAT Delta plus isotope ratio mass spectrometer. The results are reported relative to the VPDB standard by using the NBS-19 reference sample. The precision was better than ± 0.03‰ ($\delta^{13}C$).

3.4.2. Molybdenum isotopes

Molybdenum isotope compositions were determined at the IGS PAS (Kraków) for Kowala, Plan di Zermula A and Drewer samples and at PSO (Pôle de Spectrométrie Océan, Plouzané, France) for Kahlleite and Kronhofgraben samples. The analytical protocols for the chemical digestion and purification of Mo from all shale powders are described in details by Duan et al. (2010) and Liermann et al. (2011). The Mo isotope compositions were measured by using a combination of the Zr element spike method and standard–sample bracketing at IGS PAS (Anbar et al., 2001), as well as the double-spike method at the PSO (Siebert et al., 2001; Asael et al., 2013) to correct for instrumental mass fractionation. The samples were analyzed at least a minimum of two times. The $\delta^{98}Mo$ values are presented relative to an in-house Mo reference solution Alfa Aesar Specpure, ICP Mo solution standard at the IGS PAS and NIST 3134 standard solution at PSO. The instrument accuracy was verified by analysing the USGS Devonian Ohio black shale standard, SDO-1, processed in the same manner as the samples. The average $\delta^{98}Mo$ for SDO-1, based on three separate powder digestions, was 1.12 (± 0.14‰, 2SD, IGS PAS) and 1.22 (± 0.09‰, 2SD, PSO; converted relative to $\delta^{98}Mo_{AA}$). The isotopic differences among the samples that were measured at the laboratories were ≤ 0.10‰. Mo isotope compositions are reported using the δ notation, where $\delta^{98}Mo$ (‰) = $[(^{98}Mo/^{95}Mo)_{sample}/(^{98}Mo/^{95}Mo)_{AA} - 1] \times 1000$, calculated relative to our in-lab Mo Alfa Aesar standard. Calibration of the Alfa Aesar standard relative to NIST3137 gave: $\delta^{98}Mo_{AA} = \delta^{98}Mo_{NIST3137} + 0.41 \pm 0.06$‰ (see also Goldberg et al., 2013).

3.5. Framboid pyrite diameter analysis

For measurements of framboid pyrite diameter environmental scanning electron microscope Philips XL30 ESEM/TMP at University of Silesia in Sosnowiec was used. Small polished slabs were analyzed in backscattered electron (BSE) mode. In each analysed samples over 100 framboids was measured if possible (as it was recommended by Wignall and Newton, 1998). However, in some samples the measurement of 100 framboid diameters was not possible. For each sample, minimum and maximum diameter, mean value and standard deviation results are presented in Supplementary Data 2.

4. Results

4.1. Mineralogical composition

Bulk mineralogical compositions of all the studied samples showed significant differences between profiles (Table 2 and Supplementary Data 1). The optimization of chemical composition of minerals is described in Supplementary Data 1.

4.1.1. Carnic Alps

The Kronhofgraben section (KR) includes the HBS, which rests between limestone units containing > 55% calcite. A similar stratigraphic succession is present for the Plan di Zermula A section (PZ), where in addition to limestones, two shale beds are present (PZ 3 and PZ 07). The dominant minerals in the HBS were determined to be quartz (22–45%) and muscovite 2M1 (14–40%). Both sections contained a significant percentage of secondary minerals in the form of goethite, and local lepidocrocite, jarosite, and/or gypsum. Pyrite (up to 12%) is present in the HBS of the KR samples. Surrounding limestone units also contained pyrite, but with only a maximum of 3%. Pyrite is less visible in the PZ samples (< 1.5%). Ankerite and dolomite comprised < 6% both in the limestone and HBS, which is a similar content to plagioclase (≤ 5%). Titanium oxides in the form of rutile and anatase comprised ~1% of the HBS samples in both sections. Optimized composition of ankerite that gives the best agreement between mineralogy and chemical analyses for KR is $CaMg_{0.71}Fe_{0.20}Mn_{0.09}CO_3$, while for PZ it is $CaFe_{0.88}Mn_{0.12}CO_3$.

The clay mineralogy in both sections is highly illitic illite–smectite (I–S) (except for muscovite 2M1). Analysis of the < 2 μm fraction of six samples indicated that this I–S contained > 90% illitic crystallites (Supplementary Data 1). The KR samples from the lower part of the HBS contained three times more I–S (in bulk) than that of the upper

Table 2
Bulk mineralogical composition of all the studied samples. HCMts - Holy Cross Mountains, HBS - Hangenberg Black Shale, SL - Sandy limestone, * > 80% illite in illite-smectite, ** ~50% illite in illite-smectite - based on analysis of < 2 um clay fraction.

	Sample	Lithology	Quartz	Kspar	Plagioclase	Calcite	Ankerite/ Dolomite	Siderite	Pyrite	Marcasite	Sphalerite	Anatase	Rutile	Goethite	Hematite	Lepidokrokite	Gypsum	Jarosite	Kaolin	Muscovite 2M1	Muscovite /illite 1M	Illite-smectite*	Smectite/ smectitic illite-smectite**	Chlorite	Biotite	SUM
Carnic Alps	KR 12C	Limestone	3.2		0.5	91.5	2.0		0.8													2.0				100.0
	KR 12B	Limestone	10.0		1.2	71.4	5.9		1.6											5.5		4.4				100.0
	KR 12A	Limestone	27.3		0.8	56.6	4.0		2.7											4.2		4.4				100.0
	KR 11	HBS	23.7		1.6				3.1			0.5	0.5	2.4						39.4	10.7	18.1				100.0
	KR 10	HBS	35.6		1.4				1.1			0.5	0.6	7.7						22.8	9.9	20.4				100.0
	KR 9	HBS	33.3			1.7	2.9		6.7			0.2	0.4	2.6						40.1	8.4	3.7				100.0
	KR 8	HBS	44.6		0.8	0.4	0.7		2.9			0.3	0.5	1.9						32.2	5.1	10.6				100.0
	KR 7	HBS	32.5		1.4		3.7		8.6			0.3	0.6							31.3	7.7	13.7				100.0
	KR 6	HBS	22.1		1.2	0.4			11.6			0.5	0.6	1.7		1.6				36.5	13.4	10.4				100.0
	KR 5	HBS	29.0		2.4				6.4											28.4		33.8				100.0
	KR 4	HBS	43.3		1.9				2.6			0.2		1.8		1.4				13.7	3.6	31.5				100.0
	KR 3	HBS	33.4		1.6	0.6			1.1			0.6	0.3	5.3						16.3	11.7	29.1				100.0
	KR 2	HBS	26.6			7.3			0.5			0.5		5.9		2.5				16.5	7.9	32.3				100.0
	KR 1	Limestone	3.9		1.2	88.9	0.9		1.0													4.1				100.0
	KR 0	Limestone	5.7			87.4	1.5		0.6													4.8				100.0
	PZ 4	Limestone	2.0		3.0	89.4	1.9		0.6													3.1				100.0
	PZ 3	Shale	16.7		3.7	3.1	2.1		1.4								0.4			18.5	11.4	42.7				100.0
	PZ 2	Limestone	3.2		2.6	88.4	1.7		0.5													3.6				100.0
	PZ 1	HBS	20.4		1.8	0.6						0.7					8.8	6.2		28.3	5.8	29.4				100.0
	PZ 0D	HBS	31.7		2.6	4.3	6.4		0.9			0.4	0.2	1.3			8.0	2.4		18.7	5.4	17.7				100.0
	PZ 0C	HBS	33.7		4.0							0.5	0.2				2.6	3.1		27.5	9.1	19.3				100.0
	PZ 0B	HBS	41.0		5.0							0.8	0.4							25.2	9.5	18.1				100.0
	PZ 0A	HBS	39.6		2.5							0.7	0.2	1.3		1.5				22.6	8.0	23.6				100.0
	PZ 02	Limestone	2.1		2.9	90.2	0.9		0.7													3.2				100.0
	PZ 03B	Limestone	1.1		1.9	92.9	0.4		0.4													3.3				100.0
	PZ 03A	Limestone	1.4		0.7	93.9	0.3		0.8													2.9				100.0
	PZ 04	Limestone	1.0		1.2	93.3	0.4		0.8													3.3				100.0
	PZ 07	Shale	8.0		0.8	11.7						0.4							0.6	23.8	12.4	42.3				100.0
Rhenish Massif	DR 8A	Shale	30.9		2.2	0.6	18.9		0.7			0.5	0.4							36.6	5.7	3.5				100.0
	DR 7C	Sandstone	42.7		4.1	0.2	13.9		0.9			0.2	0.4	0.2	0.6					31.2	5.6					100.0
	DR 7B	Sandstone	43.7	1.0	4.8	0.3	11.5		2.6			0.2	1.0							29.8	3.2	1.9				100.0
	DR 6G	HBS	32.2		2.8		1.2		0.7			0.3	0.5	1.7	0.4					47.6	6.2	6.4				100.0
	DR 6F	HBS	22.4		1.6	2.6	9.9		0.2			0.4	0.4	1.0	0.5					45.9	8.0	7.1				100.0
	DR 6E	HBS	25.3		1.1	1.4	10.7		0.0			0.4	0.5	1.1	0.5					42.1	9.2	7.7				100.0
	DR 6D	HBS	26.5		1.0	1.3	10.5		0.4			0.4	0.2	1.1	0.5					44.6	9.7	3.8				100.0
	DR 6C	HBS	29.2		1.6	1.9	10.5		0.2			0.3	0.4	1.2	0.5					42.0	6.1	6.1				100.0
	DR 6B	HBS	19.7		1.6	0.5	6.9		0.4			0.4	0.3	1.4						54.2	6.7	7.9				100.0
	DR 6A	HBS	21.1	1.0	0.4	0.7	3.0		0.4			0.4	0.4	0.7	0.6					57.9	10.3	3.1				100.0
	DR 5	Limestone	16.7		2.3	56.1	6.4		1.0											11.0	2.2	4.3				100.0
	DR 3	Limestone	7.2		1.1	76.8	4.0		0.7				0.1							7.9		2.2				100.0
	DR 0	Limestone	11.0		1.2	50.9	7.9		0.9						0.5					16.5	3.5	7.6				100.0
Thuringia	KHang 7	HBS	31.6									0.7	0.8	3.9						24.2	9.3	29.7				100.0
	KHang 6	HBS	31.9									0.9	0.6	0.0						40.4	9.8	16.4				100.0
	KHang 5	HBS	31.5						1.4			1.2	0.7	0.7						25.7	11.8	27.0				100.0
	KHang 4	HBS	30.0									1.0	0.5	0.0						31.8	13.4	23.3				100.0
	KHang 3	HBS	23.7			1.6						0.7	0.4	2.7						35.7	15.7	19.5				100.0
	KHang 2	HBS	29.9									0.7	0.3	1.4						27.7	10.0	30.0				100.0
	KHang 1	HBS	22.5									0.8	0.6	0.8						24.5	14.2	36.6				100.0
HCMts	KQ 113B	Shale	10.4	16.6		2.8			2.5			0.7							3			42.1	21.9			100.0
	KQ 112	Shale	8.4	20		9.4			0			0.6							6.9			36.2	18.5			100.0
	KQ 111	SL	50.9			17.9			0.0											2.1		29.1				100.0
	KQ 110G	HBS	44.1			0.1			2.0		0.4									2.7		48.7		2.0		100.0
	KQ 110F	HBS	22.2			31.9			1.5		0.3								2.1			26.8	15.2			100.0
	KQ 110E	HBS	8.3	1.7		14.0			2.2		0.6	0.4							3	1.7		39.3	28.8			100.0
	KQ 110D	HBS	2.4	1.3		14.2			1.1		0.6	0.6							4.3	0.0		43.5	32.0			100.0
	KQ 110C	HBS	6.9	0.4		18.4			1.9		0.4	0.3							6.2	0.0		45.9	19.6			100.0
	KQ 110B	HBS	25.9	1.8		33.0			1.9		0.9								3.7	3.1		29.7				100.0
	KQ 110A	HBS	23.1	1.8		34.0			1.1	0.8	1.1									2.7		33.4		2.0		100.0
	KQ 109G	Shale	18.8	1.8		46.7			0.9			0										29.9		1.9		100.0
	KQ 109F	Limestone	9.3			71.1			1.5			0.1								1.1		16.9				100.0
	KQ 109E	Shale	10.5	1.7		32			2			0.3								3.6		45	3.6	1.3		100.0
	KQ 109D	Limestone	0.6			64.4			0			0										30.1	4.9			100.0
	KQ 109C	Shale	11.5			29.2			0.6			0.4										44.9	13.4			100.0
	KQ 109C	Limestone	7.6			71.9			0.2													20.3				100.0
	KQ 109A	Shale	4.6			7.7			0.0	2.7		0.9							3.5			49.9	28.6		2.1	100.0
	KQ 109B	Limestone	12.0			71.9			0.3													15.8				100.0
	KQ 108B	Limestone	9.2			77.5			0.3													13.0				100.0
	KQ 106	Limestone	8.5			69.6			0.5													21.4				100.0

part (ca. 40% vs. 12–15%, respectively; Table 2). The opposite trend is recorded for muscovite 2M1 (Supplementary Data 1). In the case of the PZ, the HBS contains ca. 20% I–S, while in the two shale beds above and below the HBS the amount of I–S is two times higher (> 40%).

4.1.2. Rhenish Massif and Thuringia

Quartz and muscovite 2M1 are found to be the dominant minerals (20–32% and 42–58%, respectively) in the HBS samples from the Drewer (DR) site. The third most common mineral is 1M illite (a highly illitic I–S, up to 17%). The same minerals are also identified in underlying and overlying sandstone and limestone in significant amounts. Every HBS sample contained ~0.5–3.0% plagioclase. Iron oxides in the form of goethite and hematite are found in nearly all samples at a content of up to 2%. Among the heavy minerals, up to 1% anatase and/or rutile are present in all samples. Other components are variably represented. Ankerite and dolomite are the dominant carbonate species in the DR samples (up to 11%). Pyrite only exists in the DR samples (< 1.0%). Surrounding sandstone and limestone units generally contained the same minerals, except that some samples lacked iron and titanium oxides. The optimized composition of ankerite for DR is $CaMg_{0.78}Fe_{0.20}Mn_{0.02}CO_3$.

The HBS samples from Thuringia (Kahlleite, K-HANG) contain three dominant minerals: illite 1M polytype and highly illitic I–S (26–51%), muscovite (24–41%), and quartz (22–32%). Iron oxides are represented only by goethite (< 4%). Heavy minerals in the form of anatase and rutile comprise 1–2% of samples. Traces of calcite and pyrite are only present in one sample for each mineral: K-HANG 3 and K-HANG 5, respectively. Clay mineralogy of the < 2 μm fraction for samples K-HANG 5 and K-HANG 6 indicate > 95% of illitic crystallites in I–S. Kaolinite is also present in the samples.

4.1.3. Holy Cross Mountains

The mineralogy of the HBS samples from the Kowala (KQ) is significantly different from that of all other samples. The dominant mineral is I–S (30–69%) and contained a higher percentage of smectitic interlayers (up to 35%; Supplementary Data 1). In comparison to exposures of HBS samples from other localities, there is also a relatively large amount of calcite (up to 35%). Potassium feldspar comprised up to 2% of samples, whereas overlying samples comprised up to 20%. Sulfides, including pyrite (1–2%), marcasite (0.8% in KQ 110A), and sphalerite (0.3–1%), were also found to be important minerals. The uppermost and the lowermost horizons of the HBS contains 2% chlorite, while in the central interval there is between 2% and 6% kaolinite. Compared to HBS from other localities, there is also a lack of iron oxides and a very small content of muscovite 2M1. The surrounding rocks are mainly carbonate with scattered layers of shale, some of which contained biotite (ca. 2%, sample KQ 109A). The clay mineralogy (Supplementary Data 1) confirms the existence of chlorite and kaolinite, and indicated that there is an increasing trend in the percentage of smectitic crystallites in I–S from the upper and lower contacts towards the center of the HBS. A similar trend is also evident in the amount of muscovite, with 3% at the top and base, and almost zero in the center of the bed.

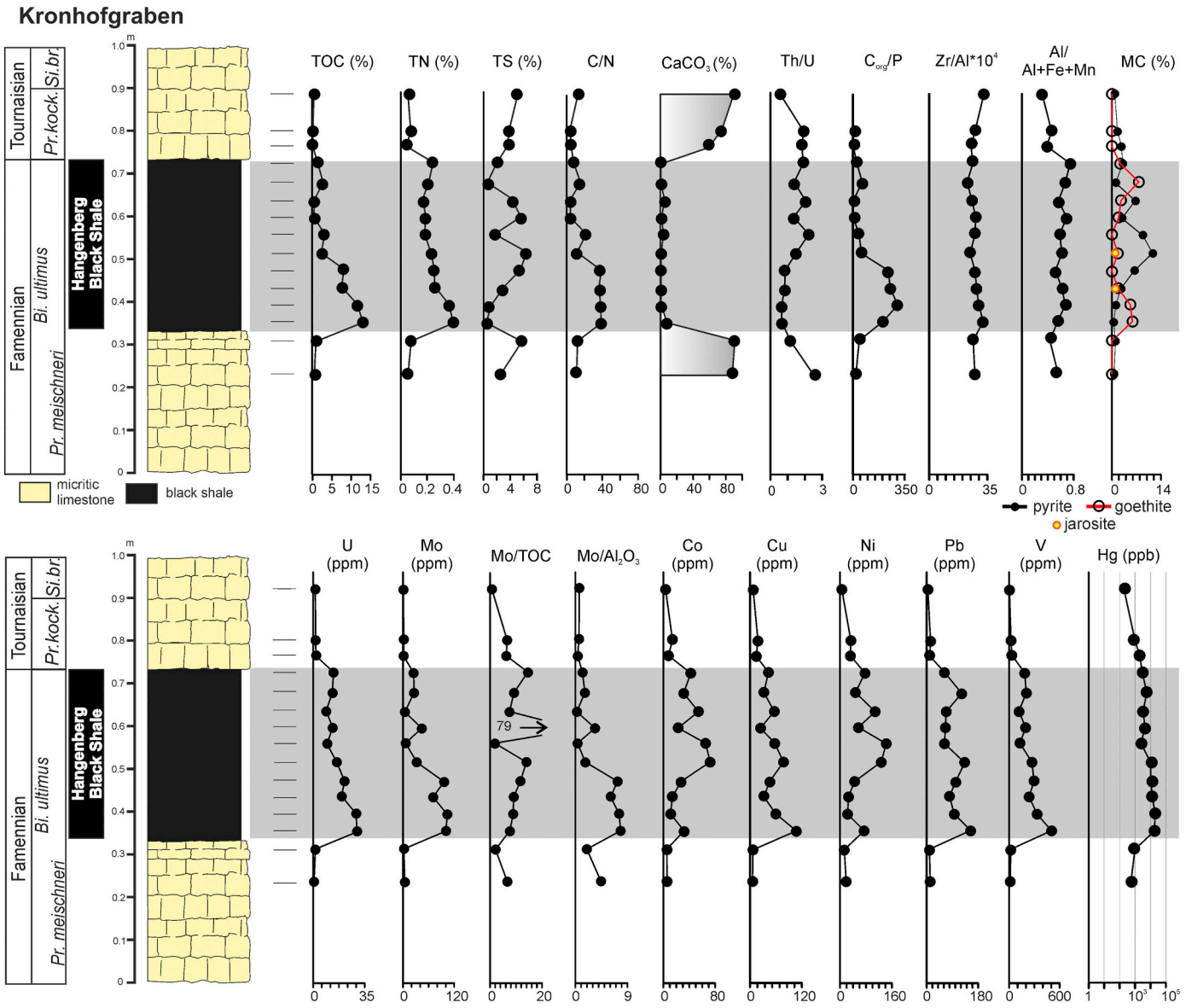

Fig. 2. Whole rock geochemistry of the Hangenberg Black Shale interval at Kronhofgraben (Carnic Alps) and selected mineral components (MC).

4.2. Geochemical composition

Detrital input was estimated based on Si/Al, Zr/Al, K/Al, and Ti/Al ratios (e.g., as undertaken by Pujol et al., 2006; Tribovillard et al., 2006; Rakociński et al., 2018). Redox conditions were assessed based on Th/U, C_{org}/P, and V/Cr ratios and Mo contents (e.g., see Bond et al., 2004; Rimmer, 2004; Rakociński et al., 2018). Rocks that formed in anoxic environments are characterized by an enrichment of redox-sensitive trace metals such as U, Mo, Zn, Pb, Ni, Cu, Cd, and V (e.g., Tribovillard et al., 2006; Calvert and Pedersen, 2007), and the enrichment factors are highlighted recently as the most reliable redox proxies by Algeo and Liu (2020).

All lithogenic elements, such as Si, K, Ti, and Zr, in almost all of the investigated sections exhibit strong positive correlations with Al. Therefore, these elements could be used as proxies for detrital input (for more information and details see Tables 3–7 and Supplementary Data 1). The exception is the Kahlleite section, where Si, Zr, and Ti showed no correlation with Al and only a moderate correlation for K (Supplementary Data 1). For this reason, Si could not be used as a productivity proxy in the studied sections (see Racki et al., 2002; Rakociński et al., 2018). According to Ver Straeten et al. (2011), Si/Al values > 5 indicate a dominant influx of sandy fractions. This SiO_2 enrichment probably reflects the record of the global trend associated with the regression represented in the Rhenish Massif by coarser clastic strata (i.e., the Hangenberg Sandstone and its equivalents; Kaiser et al., 2011).

Th/U ratios in almost all investigated samples from the HBS interval have values < 3 (Figs. 2–6, Tables 3–7). Elevated V/Cr ratios (> 4.25) existed only in a few samples from the Kowala (Table 7). Mo concentrations in the HBS interval in the Kronhofgraben fluctuated between 3.8 and 103.6 ppm, with an average enrichment factor (EF_{Mo}) of 70.53 (Table 3, Supplementary Data 3). While in the Plan di Zermula A, the Mo concentration of in the HBS interval ranges from 3.2 to 72.5 ppm, with an average EF_{Mo} of 34.48 (Table 4, Supplementary Data 3). In the Drewer quarry, the Mo concentration in the HBS interval range between 16.4 and 41.6 ppm, with an average EF_{Mo} of 33.22 (Table 5, Supplementary Data 3), which is very similar to the Thuringia HBS samples that have average EF_{Mo} values of 34.29 (Table 6, Supplementary Data 3). Higher Mo concentrations in the HBS interval were detected in the Kowala section (7.9–161.2 ppm), where the average EF_{Mo} is 94.71 (Table 7, Supplementary Data 3). In many worldwide sections, the anoxic intervals are enriched in redox sensitive elements (e.g. U, V, Cr, Ni, Pb, Zn and Cu) and depleted in Mn (cf. Brumsack, 2006;

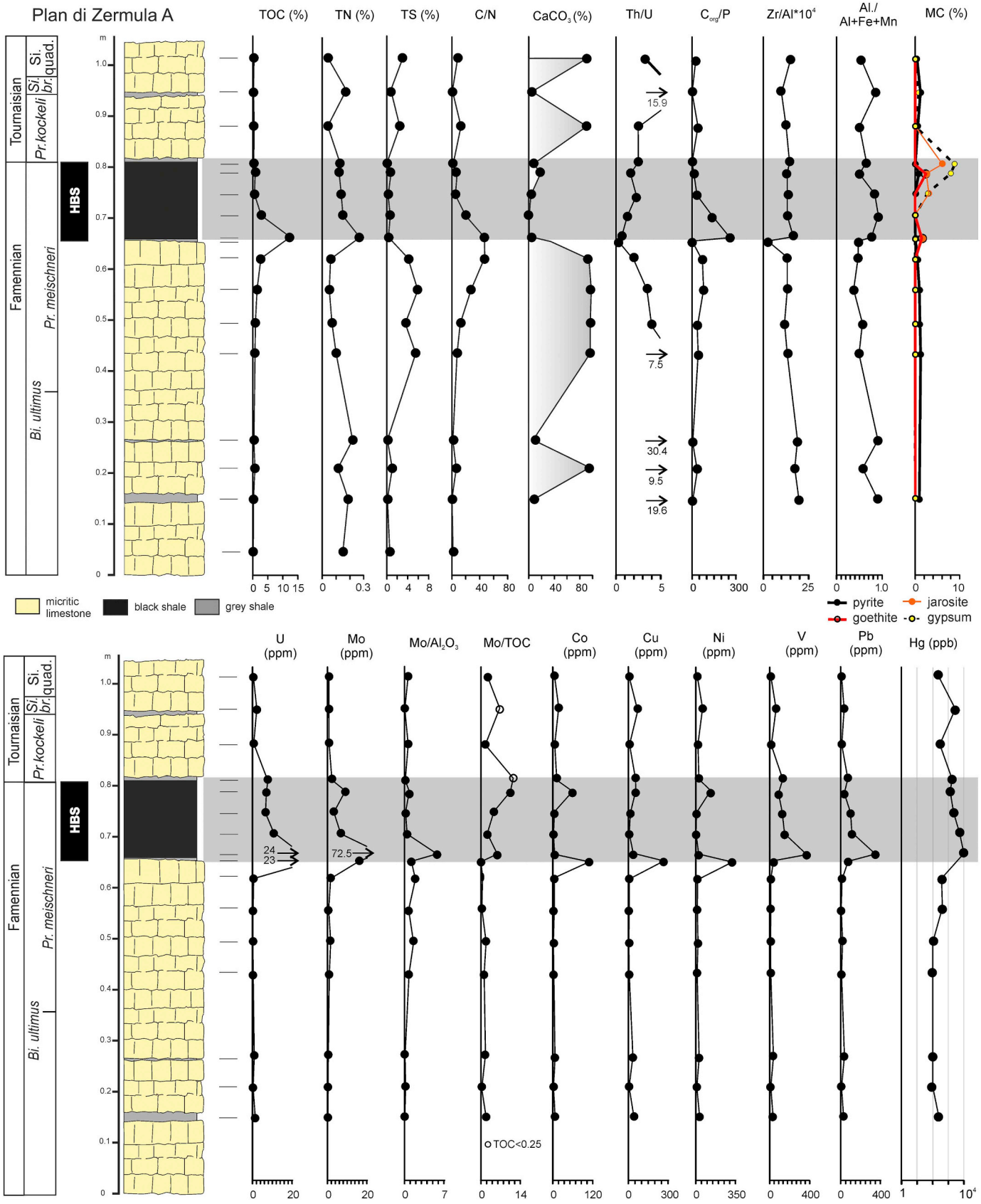

Fig. 3. Whole rock geochemistry of the Hangenberg Black Shale interval at Plan di Zermula A (Carnic Alps) and selected mineral components (MC). Abbreviation: HBS – Hangenber Black Shale.

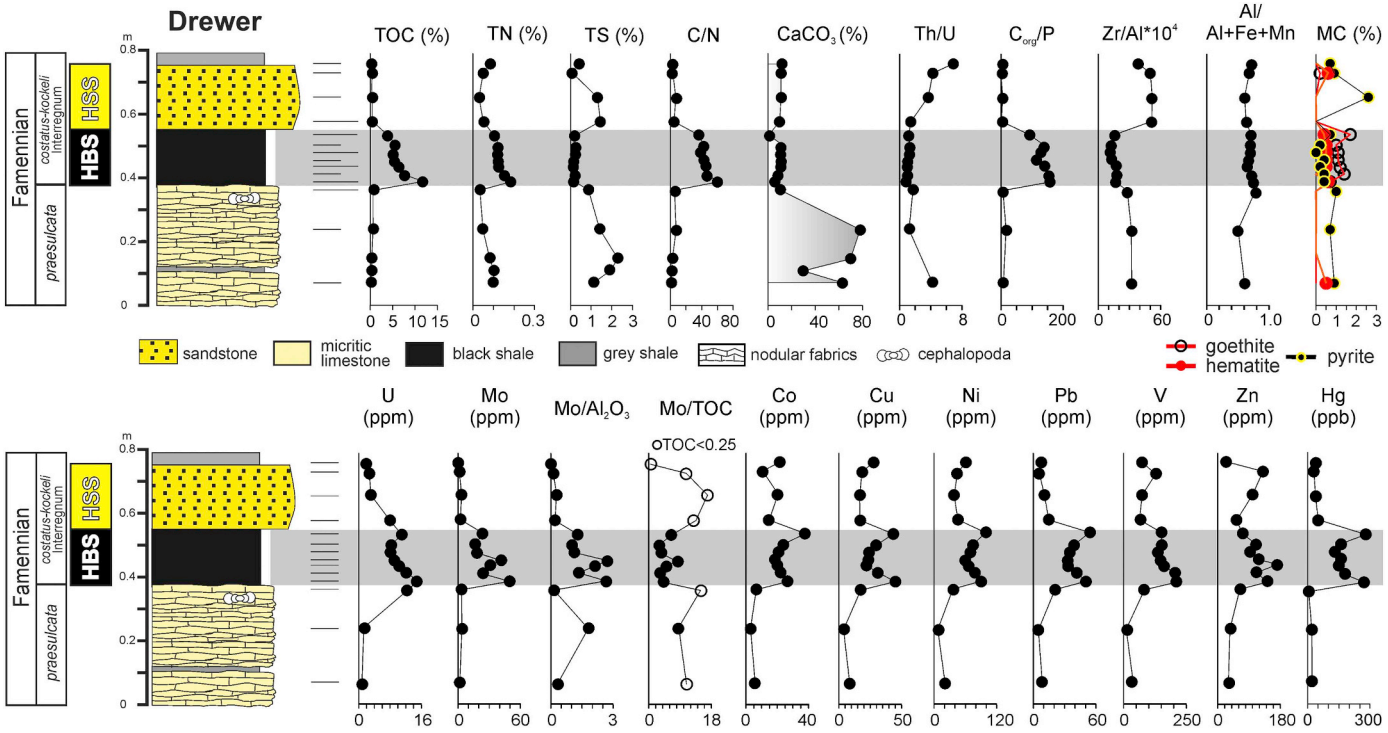

Fig. 4. Whole rock geochemistry of the Hangenberg Black Shale interval at Drewer section (Rhenish Massif) and selected mineral components. Abbreviation: HBS – Hangenberg Black Shale, HSS – Hangenberg Sandstone.

Tribovillard et al., 2006; Calvert and Pedersen, 2007; Rakociński et al., 2018; Derkowski and Marynowski, 2018). Generally, the HBS interval in the studied sections is enriched in U, V, Cr, and Ni (with the exception of the Kahlleite section), and depleted in Mn (with exception of the Kowala; see Tables 3–7). The highest enrichment in redox sensitive trace metals is in samples from the HBS of the Kowala site (avg. EF_V = 4.30; avg. EF_{Cu} = 7.07; avg. EF_{Pb} = 106.59; avg. EF_{Zn} = 329.59; EF_{Ni} = 8.84; EF_{Cr} = 4.35, and avg. EF_{Mn} = 5.72). Total organic carbon and total nitrogen content results are discussed in Supplementary Data 1 section.

4.3. Isotopic changes: bulk sediment C and Mo isotopic compositions

4.3.1. $\delta^{13}C$

A negative shift in $\delta^{13}C_{org}$ values across the HBS exist in the Kowala, Drewer, Kahlleite, Kronhofgraben and Plan di Zermula A sections, and a slightly increasing trend in values within the HBS for all of these sections (Fig. 7, Tables 3–7). For the DR, PZ, KR, and KQ, black shale is ^{13}C-depleted by 1.5‰, 2‰, 3‰, and 4‰, respectively, relative to the immediately underlying and overlying strata. A positive excursion is

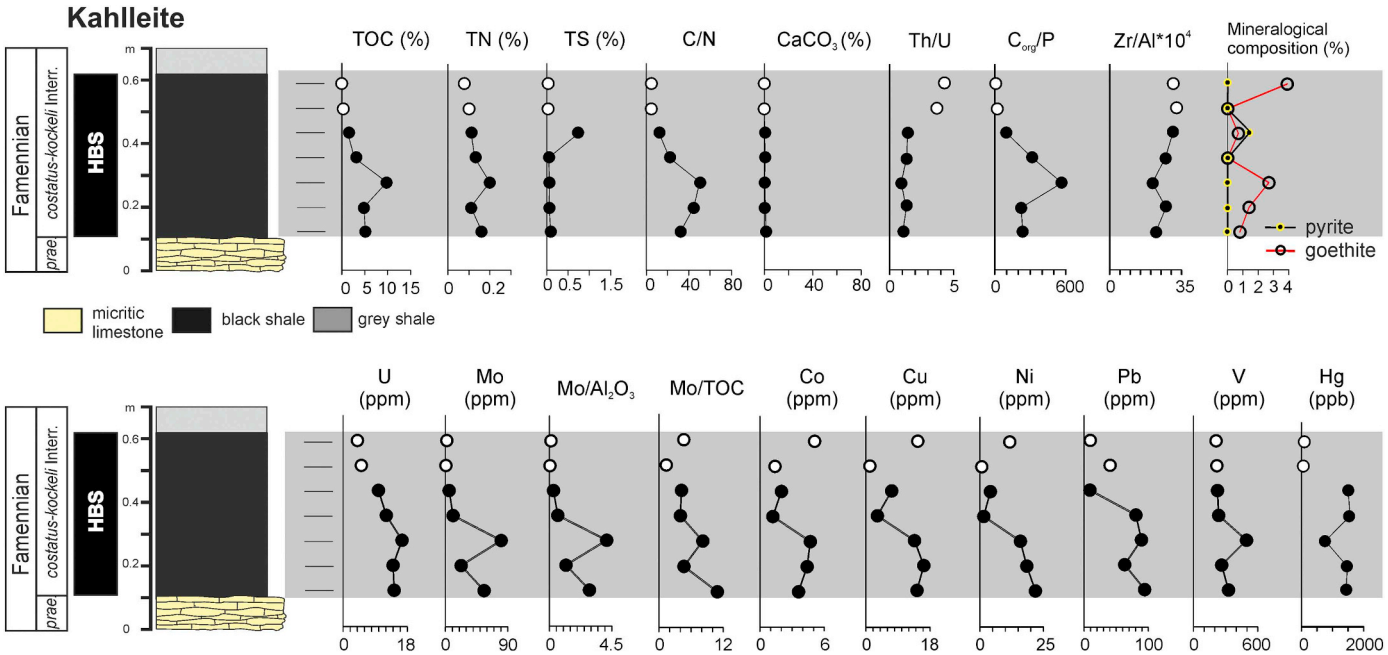

Fig. 5. Whole rock geochemistry of the Hangenberg Black Shale interval at Kahlleite (Thuringia) and selected mineral components. White dots marked the weathered samples.

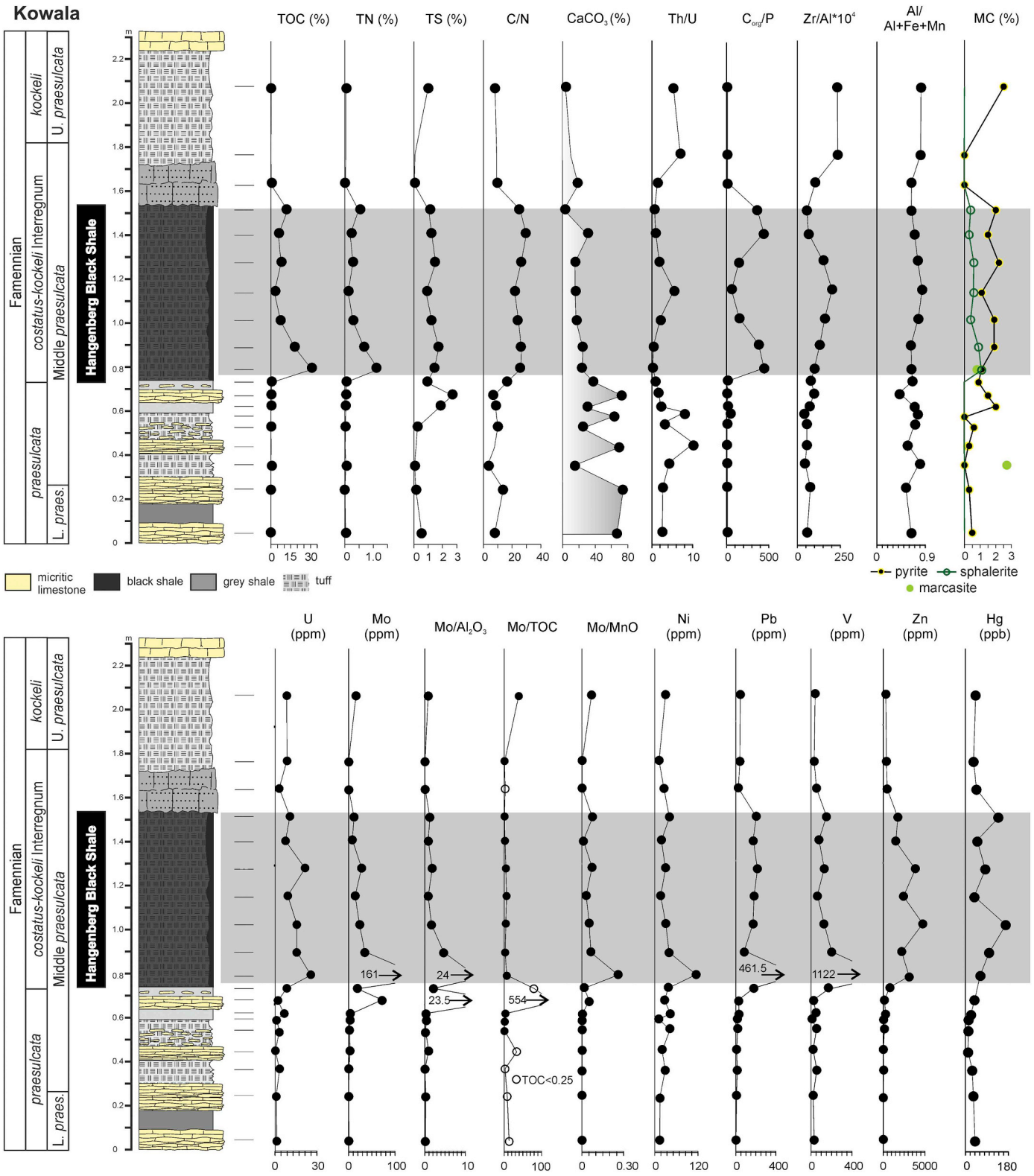

Fig. 6. Whole rock geochemistry of the Hangenberg Black Shale interval at Kowala (Holy Cross Mountains) and selected mineral components. Conodont biostratigraphy after Woroncowa-Marcinowska (2017).

defined by the rising values in the upper part of the HBS (PZ), a peak just above the HBS, and a subsequent decline in values (Fig. 7). There is no significant correlation between $\delta^{13}C_{org}$ and TOC for the PZ ($r = -0.38$) and K-HANG ($r = -0.20$) sections, and a moderate negative correlation for the DR ($r = -0.69$), KR ($r = -0.62$), and KQ ($r = -0.79$) sites.

Isotopic trends of inorganic C ($\delta^{13}C_{carb}$) in the KQ mimic those of $\delta^{13}C_{org}$ (Fig. 7). The $\delta^{13}C_{carb}$ values obtained below the HBS are ~1‰ (background level). At the base of the black shale facies, $\delta^{13}C_{carb}$ decreases to −1.3‰. Throughout the HBS, C isotopes gradually increased and reach 1.1‰ in the first layer above the HBS.

Table 3
Geochemical data in the samples of Kronhofgraben section. Blue – oxic conditions, pale yellow – dysoxic conditions, grey – anoxic conditions. Colours of samples (black – Hangenberg black shales; blue – limestone), n.d. – no data, b.d. – below detection.

	Sample	TOC	TS	TN	$CaCO_3$	Th	U	Mo	V	P	Hg	Uauth	Th/U	C_{org}/P	Si/Al	K/Al	Ti/Al	Zr/Al*10^4	Al/(Al+Fe+Mn)	Fe/Ti	$\delta^{13}C_{org}$	δ^{98}Mo	
		[%]	[%]	[%]	[%]	[ppm]	[ppm]	[ppm]	[ppm]	[%]	[ppb]										‰	‰	2SD
	KR 12C	0.57	4.94	0.06	88.97	0.7	1.2	0.4	b.d.	b.d.	221	0.97	0.58	b.d.	6.43	0.36	0.07	32.84	0.31	19.54	-25.7	n.d.	n.d.
	KR 12B	0.2	3.77	0.09	92.27	2.7	1.4	1.3	23	0.013	864	0.50	1.93	15.28	6.16	0.48	0.08	27.80	0.46	13.50	-26.0	n.d.	n.d.
	KR 12A	0.13	3.55	0.03	8.17	3.1	1.7	0.8	31	0.013	1957	0.67	1.82	9.93	14.24	0.46	0.07	25.55	0.39	20.23	-23.9	n.d.	n.d.
HANGENBERG BLACK SHALE	KR 11	1.67	2.05	0.23	0.73	22.5	11.8	24.3	184	0.065	3288	4.30	1.91	25.51	2.57	0.47	0.08	26.09	0.75	4.45	-27.3	1.03	0.09
	KR 10	2.78	0.65	0.21	0.25	15.6	11.3	25.4	205	0.044	5695	6.10	1.38	63.70	3.56	0.46	0.07	23.13	0.67	6.94	-27.4	1.78	0.06
	KR 9	0.51	4.10	0.17	0.12	15.3	7.5	3.8	118	0.052	3377	2.40	2.04	9.74	3.56	0.47	0.07	25.77	0.57	10.13	-25.1	1.99	0.07
	KR 8	0.55	5.70	0.19	0.34	15.2	11.3	43.4	195	0.048	4453	6.23	1.35	11.46	4.60	0.47	0.08	28.01	0.69	5.79	-27.3	1.51	0.07
	KR 7	3.22	1.79	0.18	3.48	18.2	8.2	5.8	128	0.087	2625	2.13	2.22	36.89	3.25	0.46	0.07	27.51	0.59	8.99	-25.2	n.d.	n.d.
	KR 6	2.28	6.32	0.23	1.02	20.3	13.7	31.8	271	0.039	12107	6.93	1.48	58.05	2.46	0.45	0.07	24.55	0.62	8.43	-27.2	1.93	0.06
	KR 5	8.26	5.49	0.25	4.82	14.9	18.2	96.1	296	0.035	13150	13.23	0.82	236.59	3.50	0.45	0.07	27.49	0.52	12.40	-27.4	1.61	0.07
	KR 4	7.72	2.15	0.25	0.37	14	16.6	70.2	237	0.031	12894	11.93	0.84	252.72	4.73	0.44	0.07	28.42	0.63	8.17	-27.3	1.64	0.07
	KR 3	11.78	1.06	0.37	0.45	16.3	25	103.6	332	0.039	20216	19.57	0.65	299.93	3.58	0.42	0.07	29.70	0.68	6.70	-27.6	2.21	0.09
	KR 2SP	13.28	0.46	0.40	60.11	17.1	25.5	100.4	504	0.065	18466	19.80	0.67	202.87	3.26	0.44	0.07	32.24	0.56	11.62	-27.9	1.87	0.06
	KR 1	1.03	5.78	0.09	75.96	1.5	1.3	2.1	19	0.022	914	0.80	1.15	47.20	4.06	0.34	0.06	26.31	0.45	16.92	-26.5	1.54	0.06
	KR 0	0.62	2.49	0.06	94.34	1.3	0.5	4.1	13	0.031	611	0.07	2.60	20.30	7.42	0.44	0.06	27.43	0.51	13.30	-25.1	n.d.	n.d.

4.3.2. δ^{98}Mo

The Mo isotope values in the Carnic Alps range from 1.5 to 2.2‰ in the Kronhofgraben section, and from 0.8 to 1.7‰ in the Plan di Zermula A section. Decreases to 1.0‰ (KR) and 0.3‰ (PZ) are present in the top of the HBS (Fig. 8, Tables 3–4). The δ^{98}Mo values for the HBS samples from the Rhenish Massif (DR) and Thuringia (K-HANG) range from 0.8 to 1.2‰ and 0.2 to 1.2‰ (Fig. 8, Tables 5–6), respectively. There are lower δ^{98}Mo values (~0‰) in the upper part of the HBS in the Kahlleite. The δ^{98}Mo values decrease to 0.7‰ in the Hangenberg Sandstone in the Drewer. The δ^{98}Mo record in the Holy Cross Mountains show a similar pattern to that of the Rhenish Massif and the Carnic Alps (Fig. 8, Table 7). Samples in lower part of the HBS in the Kowala (KQ 110A–KQ 110C) show the highest values (average 1.46 ± 0.07 ‰). The middle and upper parts of the black shale (KQ 110D–KQ 110G) record δ^{98}Mo values that ranged from 1.0 to 1.5‰ (average 1.21 ± 0.21‰). Pearson's correlation was used to compare δ^{98}Mo with the geochemical data (Supplementary Data 1).

4.4. Framboidal pyrite

Among the 15 samples analyzed from the Kronhofgraben (10 samples encompassed the HBS interval) only 5 contained framboids (Fig. 9, Supplementary Data 2). Only one hundred measurements were possibly in two samples. In the other samples, the frequency of framboids was low or framboids were absent. In all samples, euhedral pyrite crystals (in variable abundance) are present. In the lowermost sample (KR 2) small framboids (< 5 μm) predominate (Fig. 9) and larger forms (> 10 μm) are rare. In the other positive sample, small framboids (< 5 μm) are also present, but in a lower frequency, and the sample are dominated by euhedral pyrite crystals. In the Plan di Zermula A, in all samples pyrite framboids are absent, possibly due to modern weathering (see Section 5). In the Drewer samples, framboids are present in 7 of the 11 analyzed samples (Fig. 9, Supplementary Data 2). All samples from the HBS interval contained numerous framboids, which are mostly small (Fig. 9), although larger forms (> 5 μm) also exist in all samples. Very large framboids (> 10 μm) are present in three samples. In the Kahlleite samples, all seven were devoid of framboids due to weathering (Supplementary Data 2). Some euhedral crystals of pyrite are present only in sample K-HANG-3. The distribution of pyrite framboids in the HBS at the Kowala quarry was described in detail by Marynowski et al. (2012). All investigated samples are rich in framboids and dominated by small (< 5 μm) framboids with little variation in size.

5. Weathering and diagenetic alteration

The degree of weathering of the studied sections is reflected by the content of specific elements, including Mo, Cu, Zn, As, Sb, and Co, which accumulated in sulfide minerals and organic matter (Algeo and Liu, 2020). Generally, weathered black shale samples have much lower concentrations of chalcophile elements in comparison to nonweathered samples (cf. Marynowski et al., 2017). Weathering may also be recorded by a lack of framboids and pyrite crystals, which are replaced by FeOOH (see Marynowski et al., 2011; Mahoney et al., 2019) or gypsum and jarosite (as secondary products of reaction of iron[II] sulphate and sulphuric acid, produced by pyrite oxidation, with carbonate and clay minerals) (Forster et al., 1995).

A few samples from the Carnic Alps, Rhenish Massif and Thuringia sections contain goethite or hematite (generally < 3%), thus indicating either (i) an input of these minerals during the deposition of black shale or (ii) at least partial weathering of the profiles (Figs. 2–5). Sulfate in the form of jarosite and gypsum in the Carnic Alps sections (Table 2) may also indicate weathering symptoms of coexisting pyrite. A previous study of black shale (Marynowski et al., 2017) showed that reductions in total S and Mo, in tandem with diminished Mo stable isotope values (δ^{98}Mo ~0‰), may be used for assess the degree of weathering. This relationship holds for samples K-HANG 6 and K-KANG 7 (Kahlleite) and PZ 0D sample (Plan di Zermula A). High percentages of goethite and low amount of pyrite at the base and top of the HBS in Kronhofgraben in comparison to the middle of the bed may indicate a minor degree of weathering in the uppermost and the lowermost of the HBS layer. This

Table 4
Geochemical data in the samples of Plan di Zermula A section. Refer to Table 3.

	Sample	TOC	TS	Th	U	Mo	V	P	Hg	Uauth	Th/U	C_{org}/P	V/Cr	Si/Al	K/Al	Ti/Al	Zr/Al*10^4	Al/(Al+Fe+Mn)	Fe/Ti	$\delta^{13}C_{org}$	δ^{98}Mo	
		[%]	[%]	[ppm]	[ppm]	[ppm]	[ppm]	[%]	[ppb]											‰	‰	2SD
	PZ 4*	0.33	3.03	1.3	0.4	0.8	12	0.01	223	-0.03	3.25	25.21	0.16	3.86	0.23	0.05	28.42	0.53	13.03	-25.88	n.d.	n.d.
	PZ 3	0.12	0.72	35	2.2	0.8	72	0.07	2807	-9.47	15.91	1.83	1.50	2.10	0.43	0.03	18.33	0.86	6.31	-27.34	n.d.	n.d.
	PZ 2*	0.52	2.36	1.5	0.6	0.8	17	0.01	305	0.10	2.50	39.72	0.18	4.66	0.26	0.06	23.51	0.50	12.17	-27.24	n.d.	n.d.
	PZ 1	0.20	0.12	19.1	7.7	2.3	147	0.07	1745	1.33	2.48	2.86	1.02	2.83	0.46	0.07	27.39	0.65	7.82	-25.61	n.d.	n.d.
HBS	PZ 0D	0.87	0.81	11.5	7	9.1	100	0.06	1345	3.17	1.64	14.24	1.62	4.14	0.42	0.07	24.33	0.50	12.94	-26.40	0.32	0.18
	PZ 0C	0.70	0.31	14.9	6.6	3.2	140	0.02	2289	1.63	2.26	32.08	1.57	3.47	0.44	0.08	25.95	0.83	2.62	-26.03	1.04	0.09
	PZ 0B	2.99	0.69	13.6	10.7	6.8	167	0.02	5406	6.17	1.27	137.03	2.03	4.00	0.42	0.08	25.28	0.91	1.13	-27.33	0.94	0.34
	PZ 0A	12.53	0.38	15.8	23.8	72.5	415	0.05	9758	18.53	0.66	261.02	3.57	4.15	0.42	0.07	31.31	0.77	4.00	-27.85	1.72	0.19
	PZ01	n.d.	n.d.	6.56	22.9	16.2	44.1	0.10	391	20.71	0.29	15.00	2.21	1.00	0.07	0.01	4.83	0.48	110.60	-27.53	n.d.	n.d.
	PZ 02*	2.81	4.04	1	0.5	1.6	13	0.04	419	0.17	2.00	71.54	0.95	4.64	0.22	0.07	24.68	0.47	14.70	-27.30	n.d.	n.d.
	PZ 03B*	1.37	5.93	1.2	0.3	1.4	12	0.02	116	-0.10	4.00	36.66	b.d.	3.36	0.23	0.06	22.08	0.57	10.03	-26.51	n.d.	n.d.
	PZ 03A*	0.80	3.34	0.7	0.2	0.4	10	0.02	93	-0.03	3.50	78.48	b.d.	4.20	0.31	0.06	25.31	0.38	21.78	-26.76	n.d.	n.d.
	PZ 04*	0.77	5.49	1.5	0.2	0.8	12	0.02	102	-0.30	7.50	44.11	b.d.	2.74	0.35	0.07	25.55	0.49	13.00	-27.84	n.d.	n.d.
	PZ 05	0.28	0.08	27.4	0.9	0.4	37	0.06	87	-8.23	30.44	4.94	b.d.	1.70	0.42	0.04	35.51	0.90	2.93	-26.39	n.d.	n.d.
	PZ 06*	0.76	0.99	1.9	0.2	0.2	8	0.02	232	-0.43	9.50	34.83	0.39	2.99	0.40	0.06	32.88	0.58	12.25	-28.07	n.d.	n.d.
	PZ 07	0.11	0.02	25.5	1.3	0.2	33	0.06	223	-7.20	19.62	1.80	0.80	1.85	0.43	0.03	37.12	0.90	3.26	-27.53	n.d.	n.d.

Table 5
Geochemical data in the samples of Drewer section. Refer to Table 3.

	Sample	TOC	TS	TN	$CaCO_3$	Th	U	Mo	V	*Hg	P	Uauth	Th/U	C_{org}/P	Si/Al	K/Al	Ti/Al	Zr/Al*10^4	Al/(Al+Fe+Mn)	Fe/Ti	$\delta^{13}C_{org}$	δ^{98}Mo	
		[%]	[%]	[%]	[%]	[ppm]	[ppm]	[ppm]	[ppm]	[ppb]	[%]										[‰]	[‰]	2SD
	DR 8	0.17	0.41	0.08	11.26	13.1	1.9	0.1	73	40	0.031	-2.47	6.89	5.57	3.14	0.45	0.06	38.34	0.72	6.23	-24.5	n.d.	n.d.
	DR 7C	0.14	0.07	0.05	10.83	11.5	2.7	1.5	129	30	0.035	-1.13	4.26	4.01	4.43	0.42	0.07	49.81	0.68	6.63	-24.0	n.d.	n.d.
	DR 7B	0.19	1.34	0.03	9.42	11.4	3.1	3.2	73	40	0.035	-0.70	3.68	5.44	4.68	0.43	0.07	51.55	0.61	9.10	-23.5	0.74	0.10
	DR 7A	0.17	1.42	0.05	9.89	11.4	8	2.3	67	50	0.035	4.20	1.43	4.87	4.59	0.42	0.07	51.30	0.64	7.92	-22.9	0.75	0.18
HBS	DR 6G	3.63	0.26	0.10	0.80	12.8	11	23.4	151	280	0.039	6.73	1.16	92.42	2.84	0.46	0.05	15.91	0.71	7.44	-25.5	1.08	0.23
HBS	DR 6F	5.44	0.17	0.13	11.57	10.9	8.3	16.4	152	160	0.039	4.67	1.31	138.51	2.65	0.46	0.05	12.38	0.70	8.71	-25.3	1.01	0.20
HBS	DR 6E	5.04	0.13	0.13	10.51	10.2	8.1	18.2	136	130	0.039	4.70	1.26	128.32	2.65	0.46	0.05	11.47	0.70	8.71	-25.6	1.18	0.15
HBS	DR 6D	4.98	0.16	0.12	11.40	9.5	9.1	41.6	147	160	0.044	5.93	1.04	114.12	2.80	0.46	0.05	12.91	0.67	9.85	-25.6	1.05	0.18
HBS	DR 6C	6.13	0.18	0.13	9.74	10.2	10.3	31	161	150	0.044	6.90	0.99	140.47	3.06	0.46	0.05	17.26	0.65	10.20	-25.9	1.05	0.12
HBS	DR 6B	7.4	0.23	0.16	8.08	12.5	12.1	24	205	180	0.048	7.93	1.03	154.15	2.35	0.46	0.05	17.85	0.72	7.62	-25.7	0.87	0.35
HBS	DR 6A	11.66	0.15	0.19	5.80	12.2	14.8	49.7	210	270	0.074	10.73	0.82	157.17	2.11	0.48	0.05	16.75	0.75	7.00	-25.8	0.82	0.16
	DR 5	0.22	0.87	0.04	11.15	21.4	12.3	3.3	81	<10	0.035	5.17	1.74	6.30	1.87	0.48	0.04	27.89	0.79	6.95	-24.7	0.98	0.06
	DR 3*	0.46	1.39	0.06	78.39	1.9	1.5	3.9	14	20	0.026	0.87	1.27	17.57	4.55	0.47	0.06	32.23	0.50	13.37	-24.2	0.67	0.06
	DR 0*	0.15	2.35	0.08	69.77	3.8	0.9	1.6	32	20	0.022	-0.37	4.22	6.87	2.85	0.48	0.05	32.05	0.61	10.95	-25.8	0.08	0.05

*Hg was measured on ICP-MS.

may be related to low permeability and hydrophobicity of HBS, because pyrite exists in much higher concentrations in the center of the HBS bed. On the other side, existence of pyrite and lack of goethite in surrounding limestones units in the Carnic Alps (KR and PZ) may indicate deposition of these minerals during deposition.

The total illite content in R1 I–S varies from 65 to 80% in the HBS in the Kowala, i.e., the I–S is more illitic at the top and base and less illitic in the center of the HBS bed. This distribution can be explained by diagenesis of primary smectite (McCarty et al., 2009), which was probably of a volcanogenic origin. Diagenesis of clay mineral assemblages was more intensive at the margins of the bed due to low water permeability (smectite barrier properties and high hydrophobicity due to a high percentage of organic matter) and the thickness of the HBS. Small amounts of chlorite, confirmed by means of clay mineralogy, may indicate diagenetic smectite dissolution that leads to release of Fe and Mg and formation of chlorite at the top and base of the HBS layer. Kaolinite illitization at the margins of the HBS bed may have also been responsible for lack of kaolinite in samples KQ 110A and KQ 110G. These transformations did not have a major impact on the geochemical signature. Additionally, the lack of iron oxides, the existence of sulfides, and presence of such biomarkers as isorenieratane (Marynowski and Filipiak, 2007; Marynowski et al., 2012), indicate that there was no significant weathering of this section (excluding some parts described elsewhere: Marynowski et al., 2017; Derkowski and Marynowski, 2018).

Existence of ankerite/dolomite, a mineral commonly considered as a secondary mineral (forming cements), may indicate that the Kronhofgraben, Plan di Zermula A and Drewer sections underwent some degree of diagenesis. Cementation with ankeritic/dolomitic minerals was one of the first steps of diagenesis, and samples from Drewer contains even up to 19% of ankerite/dolomite, ferroan dolomite in the Drewer and Kronhofgraben sections, and ankerite in Plan di Zermula A. Samples from the DR has the most evolved chemical composition (the lowest content of Mg and Fe and the highest amount of Al in tetrahedral sheet), whereas at Kowala the composition is the most smectitic. These variations, however, can be rather connected with detrital contribution of muscovite 2M1 in the Drewer succession.

6. Variations in C and Mo isotope values

6.1. Carbon isotopes

The geological factors that control temporal variations in sedimentary $\delta^{13}C$ include episodes of intense volcanic activity that enhance pCO_2 (Weissert and Erba, 2004; Jones et al., 2016), massive release of ^{12}C-enriched CH_4 from the dissociation of gas hydrates (Dickens et al., 1995; Jahren, 2002; Beerling et al., 2002), thermogenic gas emissions (Schobben et al., 2019), and enhanced burial of ^{12}C-enriched organic matter that creates longer term changes in pCO_2 (Arthur et al., 1985).

The covariation between $\delta^{13}C_{org}$ and TOC values in the Carnic Alps, Rhenish Massif, and Holy Cross Mountains were evident when comparing immediately successive shale layers at high resolution. In contrast to previous C isotope studies of the Hangenberg interval, in all investigated sections a negative $\delta^{13}C$ shift occurs within the deposits associated with the HBS. These negative C isotope anomalies were correlated with the occurrence of organic C-rich strata (TOC > 5%). Negative $\delta^{13}C_{org}$ anomalies within black shale units are a common feature of the Middle to Late Devonian strata of the Appalachian basin (Sageman et al., 2003; Uveges et al., 2018). In some sections in the European part of Laurussia and China there are the negative excursions in both $\delta^{13}C_{carb}$ and $\delta^{13}C_{org}$ (see regional account in Table 1; Fig. 10).

The Rock Eval and biomarker data from the Holy Cross Mountains revealed that the organic carbon was of a marine origin (type II algal kerogen, with scarce terrestrial biomarkers; Marynowski et al., 2012; Derkowski and Marynowski, 2018). The HBS samples in the Kowala contains the carotenoid isorenieratene and its diagenetic products, which originated from green sulfur bacteria and 2α-methylohopane (Marynowski et al., 2012), thus identifying (cyano)bacterial activity. It is also considered that a wide range of bacterial groups are able to perform 2α-methylhopanoid biosynthesis, and elevated 2α-methylhopane index values have been linked to anoxia (Martinez et al., 2019 and references therein). Green sulfur bacteria are anaerobic phototrophs that are active in sulfidic waters, hence, their presence is considered to provide evidence of photic-zone euxinia (Koopmans et al., 1996). The C-isotope compositions of isorenieratane are quite variable, and have been reported to range between −10.7 and −27‰ (Sinninghe Damsté and Schouten, 2005; for detail of the signatures see Conway et al.,

Table 6
Geochemical data in the samples of Kahlleite section. Samples K-HANG 6 and K-HANG 7 are more weathered than the rest of samples. Refer to Table 3.

Sample	TOC	TS	TN	$CaCO_3$	Th	U	Mo	V	Hg	Uauth	Th/U	C_{org}/P	Si/Al	K/Al	Ti/Al	Zr/Al*10^4	Fe/Ti	$\delta^{13}C_{org}$	δ^{98}Mo	
	[%]	[%]	[%]	[%]	[ppm]	[ppm]	[ppm]	[ppm]	[ppb]									[‰]	[‰]	2SD
K-HANG 7	0.41	0.04	0.08	0.43	17.1	4	1.9	211	110	-1.70	4.28	7.23	2.82	0.45	0.10	30.94	5.19	-25.4	0.58	0.12
K-HANG 6	0.44	0.02	0.10	0.32	18.8	5.1	0.6	218	60	-1.17	3.69	20.16	2.97	0.47	0.10	32.52	1.07	-25.8	-0.05	0.11
K-HANG 5	1.26	0.77	0.11	0.37	14.1	9.9	5.3	224	1300	5.20	1.42	96.24	3.05	0.47	0.12	30.73	0.95	-26.5	0.78	0.06
K-HANG 4	2.75	0.05	0.13	1.04	16.1	12.1	11.0	235	1350	6.73	1.33	315.08	2.93	0.48	0.09	27.23	1.07	-26.8	0.21	0.18
K-HANG 3	9.84	0.07	0.20	0.41	15.1	16.5	80.5	495	790	11.47	0.92	563.70	2.37	0.48	0.07	20.92	2.65	-25.9	1.23	0.04
K-HANG 2	4.85	0.06	0.11	0.95	18.6	14	22.6	263	1280	7.80	1.33	222.27	2.60	0.46	0.08	27.35	2.83	-26.9	0.94	0.06
K-HANG 1	5.12	0.09	0.16	1.45	15.5	14.3	55.8	327	1380	9.13	1.08	234.65	2.58	0.46	0.08	22.59	2.40	-26.6	0.69	0.05

Table 7
Geochemical data in the samples of Kowala section. Refer to Table 3.

	Sample	TOC	TS	TN	$CaCO_3$	Th	U	Mo	V	Hg	Uauth	Th/U	C_{org}/P	Si/Al	K/Al	Ti/Al	Zr/Al*10^4	Al/(Al+Fe+Mn)	Fe/Ti	$\delta^{13}C_{org}$	$\delta^{13}C_{carb}$	δ^{98}Mo	
		[%]	[%]	[%]	[%]	[ppm]	[ppm]	[ppm]	[ppm]	[ppb]										[‰]	[‰]	[‰]	2SD
	KQ113B#	0.3	1.33	0.04	3	51.6	9.8	12.6	33	43	-7.40	5.27	4.89	2.48	0.45	0.07	231.62	0.82	3.34	-27.9	b.d.	n.d.	n.d.
	KQ 112#	0.4	0.05	0.04	10	70	10	< 2	31	34	-13.33	7.00	7.07	2.50	0.42	0.08	234.43	0.81	3.09	-27.6	n.d.	n.d.	n.d.
	KQ 111#	0.2	0.04	0.02	19	5	3.4	4.4	53	46	1.73	1.47	8.71	7.77	0.41	0.06	104.17	0.64	9.92	-25.2	1.1	n.d.	n.d.
HBS	KQ110G	12.5	1.39	0.48	1	8.6	12.4	11.7	150	138	9.53	0.69	358.90	5.72	0.42	0.06	55.21	0.64	10.18	-28.2	b.d.	1.21	0.12
HBS	KQ110F	5.7	1.67	0.19	31	8.4	8.7	7.9	77	50	5.90	0.97	436.91	3.92	0.35	0.04	65.97	0.70	10.08	-28.1	0.9	1.49	0.13
HBS	KQ110E	7.6	2.03	0.29	15	46.3	25.0	28.0	129	83	9.57	1.85	144.55	2.43	0.41	0.06	151.95	0.76	5.30	-28.5	0.4	1.02	0.13
HBS	KQ110D	2.6	1.13	0.12	15	58.5	10.6	14.2	62	38	-8.90	5.52	59.81	2.07	0.36	0.06	201.93	0.84	3.20	-28.5	0.2	1.10	0.14
HBS	KQ110C	7.2	1.68	0.29	16	39.5	18.1	24.1	125	169	4.93	2.18	149.99	2.45	0.40	0.06	160.17	0.77	5.30	-28.9	-0.2	1.43	0.15
HBS	KQ110B	18.2	2.32	0.68	25	7.8	18.0	34.8	201	99	15.40	0.43	379.34	4.93	0.48	0.06	130.11	0.63	10.41	-29.4	-0.7	1.54	0.24
HBS	KQ110A	30.9	1.90	1.18	24	7.8	29.8	161.2	1122	63	27.20	0.26	442.83	4.11	0.50	0.06	100.56	0.64	8.78	-30.1	-1.3	1.40	0.13
	KQ109G#	0.5	1.19	0.03	40	9	9.8	19	169	38	6.80	0.92	12.22	3.70	0.49	0.06	78.16	0.66	7.94	-26.2	n.d.	n.d.	n.d.
	KQ109F*#	0.3	3.60	0.04	72	3.9	2.4	82.5	25	24	1.10	1.63	4.91	4.71	0.47	0.06	97.57	0.42	20.52	-25.8	0.0	n.d.	n.d.
	KQ109E	0.5	n.d.	n.d.	29	17.7	7.7	3.7	49	14	1.80	2.30	13.50	2.74	0.49	0.05	71.80	0.70	8.73	n.d.	n.d.	n.d.	n.d.
	KQ 109D	0.4	n.d.	n.d.	62	9.7	1.2	3.3	10	13	-2.03	8.08	46.35	1.97	0.37	0.02	40.26	0.76	11.81	n.d.	n.d.	n.d.	n.d.
	KQ 109C	0.2	0.35	0.02	25	11.5	3.6	1.9	54	11	-0.23	3.19	6.55	2.89	0.49	0.05	55.40	0.71	8.19	-26.4	1.3	n.d.	n.d.
	KQ109B*#	0.2	0.22	0.02	69	2.8	1.1	2.2	20	28	0.17.	1.82	1.72	5.43	0.47	0.06	55.16	0.57	10.77	-26.8	0.9	n.d.	n.d.
	KQ 109A	0.2	0.07	0.05	15	25.7	0.8	0.6	115	38	-7.77	32.13	4.91	2.17	0.41	0.08	43.86	0.80	2.96	-26.4	n.d.	n.d.	n.d.
	KQ108B*#	0.1	0.19	0.01	75	2.7	1	0.8	21	34	0.10	2.70	3.56	5.43	0.46	0.06	74.71	0.54	11.59	-26.4	0.7	n.d.	n.d.
	KQ106*#	0.2	0.77	0.03	66	3.6	1.4	< 2	30	40	0.20	2.57	9.17	3.73	0.51	0.05	57.29	0.64	9.72	-26.3	1.1	n.d.	n.d.

#Data from ACTLabs.

1994; Hollander and Smith, 2001; Takahashi et al., 2010).

Cyanobacterial benthic mats, recognized in thin sections from the HBS, existed during seasonal and/or temporal bottom-level oxygenation states (Kazmierczak et al., 2012). In the HBS, cyanobacteria formed the top layer of massive benthic microbial mats, while chemotrophic organisms degraded the underlying cyanobacterial biomass, thus producing H_2S (cf. Kazmierczak et al., 2012). Increased photosynthetic carbon isotope fractionation under high $[CO_2]_{aq}$ conditions in the surface ocean above the chemocline in addition to increased chemoautotrophic carbon fixation at and below the chemocline, could have driven a negative shift in $\delta^{13}C_{org}$ during deposition the HBS.

6.2. Mo isotope

Mo isotope signatures of marine strata are largely controlled by the redox conditions in the water column (Siebert et al., 2006). In oxic water masses, Mo, as molybdate, is scavenged by oxidized Mn and Fe oxyhydroxides, or other mineral phases. The isotope compositions of marine ferromanganese phases are light (δ^{98}Mo < 0‰; Siebert et al., 2003; Nägler et al., 2005;). In dysoxic conditions, Mo fractionation results in δ^{98}Mo values from approximately 0.8–2.2‰ (Goldberg et al., 2009), with typical values of ~1‰ (Siebert et al., 2006). Under anoxic and euxinic environments, when there are sulfidic conditions in sediment pore waters or in the water column, the molybdate ion is converted into reactive thiomolybdate species and is subsequently incorporated into sulphides or scavenged by S-rich organic matter (Neubert et al., 2008; Helz and Vorlicek, 2019). In strongly euxinic water columns, in which free H_2S exceeds 11 μM, sediment can preserve δ^{98}Mo values close to that of modern seawater (i.e., δ^{98}Mo = 2.34 ± 0.10‰; Barling et al., 2001; Nakagawa et al., 2012). However, several factors including pH, S speciation, and $[H_2S]_{aq}$ concentrations could affect the rate of Mo removal to sediments in O_2-poor marine environments, and may cause non-quantitative Mo removal from the water column (e.g., Nägler et al., 2011). Therefore, in basins where bottom waters are weakly or intermittently euxinic, the underlying sediments has δ^{98}Mo values of between −0.6 and 1.8‰, with heavier Mo isotope compositions generally occurring at higher $[H_2S]_{aq}$ (Arnold et al., 2004; Nägler et al., 2005; Kendall et al., 2011). Additionally, fluctuations in the δ^{98}Mo record may indicate blooms of specific primary producers and input of Mo from terrestrial or hydrothermal sources to anoxic basins. Zerkle et al. (2011) demonstrated that N_2-fixing cyanobacteria can produce large fractionations in δ^{98}Mo, and could have provided an important source of isotopically-light Mo bound to organic matter, particularly in anoxic sedimentary environments.

Most δ^{98}Mo data for the HBS were dispersed within the range of characteristic of reducing conditions (1.0–1.5‰ in the Holy Cross Mountains, ~1‰ in the Rhenish Massif, 0.7–1.2‰ in Thuringia, and 0.8–2.2‰ in the Carnic Alps). In the upper part of the HBS in Thuringia and Kronhofgraben section, Mo concentrations and isotope ratios were depleted (–0.1 to 0.8‰ and to 1.0‰, respectively) in comparison to those of the bottom part of the shale bed. The same holds true for the Plan di Zermula A, where δ^{98}Mo values in the upper part of the HBS are lower (0.3 ‰) in comparison to that of the bottom and middle parts of the shale. The Famennian Chattanooga Shale and the Clegg Creek Member of the New Albany Shale (with depositional ages of between 374.5 and 359.2 Ma) have δ^{98}Mo values of 1.45–1.66‰ and 1.73–1.93‰, respectively (Dahl et al., 2010). While, the lower black shale member of the Exshaw Formation (Western Canadian Sedimentary Basin) which was deposited during the Devonian–Mississippian boundary interval (depositional age constrained between 363 and 360

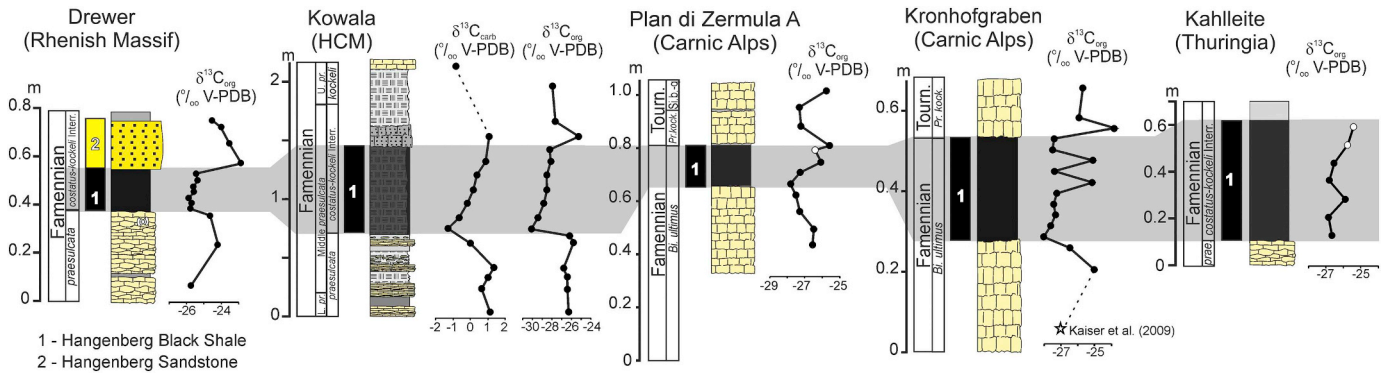

Fig. 7. Interregional correlation of the Hangenberg Black Shale interval from the northern Rhenish Massif (Drewer) with the Holy Cross Mountains (Kowala), Carnic Alps (Plan di Zermula A, Kronhofgraben), and Thuringia (Kahlleite), based on δ^{13}C curves.

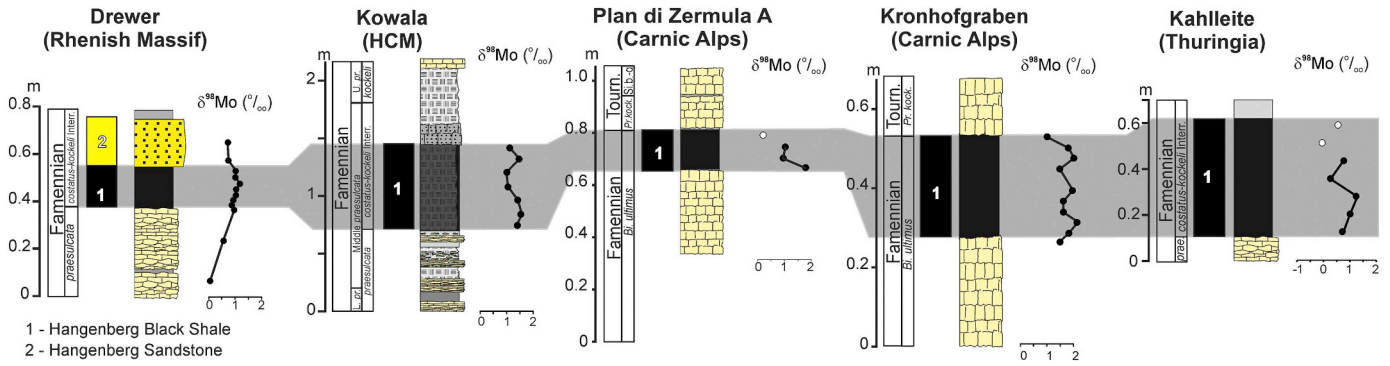

Fig. 8. Interregional correlation of the Hangenberg Black Shale interval from the northern Rhenish Massif (Drewer) with the Holy Cross Mountains (Kowala), Carnic Alps (Plan di Zermula A, Kronhofgraben), and Thuringia (Kahlleite), based on δ^{98}Mo curves.

Ma; Tucker et al., 1998; Creaser et al., 2002) in euxinic bottom water has δ^{98}Mo values ranging from 0.3‰ to 1.1‰ (Yang, 2019).

The δ^{98}Mo values indicate that the shale was deposited in weakly ($H_2S < 11$ mM) to strongly ($H_2S > 11$ mM) euxinic conditions (Dahl et al., 2010). The studied HBS were deposited in basins that had a relatively good connection to open oceans (Rheic and Paleo-Tethys oceans), similar to the modern, moderately restricted Venezuelan Cariaco Basin (see Chapter 7). Hence, the dispersion of δ^{98}Mo values recorded in the studied sections may be interpreted as a result of changes in paleoredox conditions in the water column (Siebert et al., 2006; Gordon et al., 2009). In addition, by analogy to the Cariaco Basin, the dispersion in values may record inefficient Mo reduction with high Mo isotope fractionation, or delivery of isotopically light Mo from the operation of an Fe–Mn oxide particulate shuttle (Brüske et al., 2020; Helz and Vorlicek, 2019).

7. Geochemical signatures of anoxia, volcanic input and hydrothermal activity

Deep-marine deposits affected by hydrothermal processes have

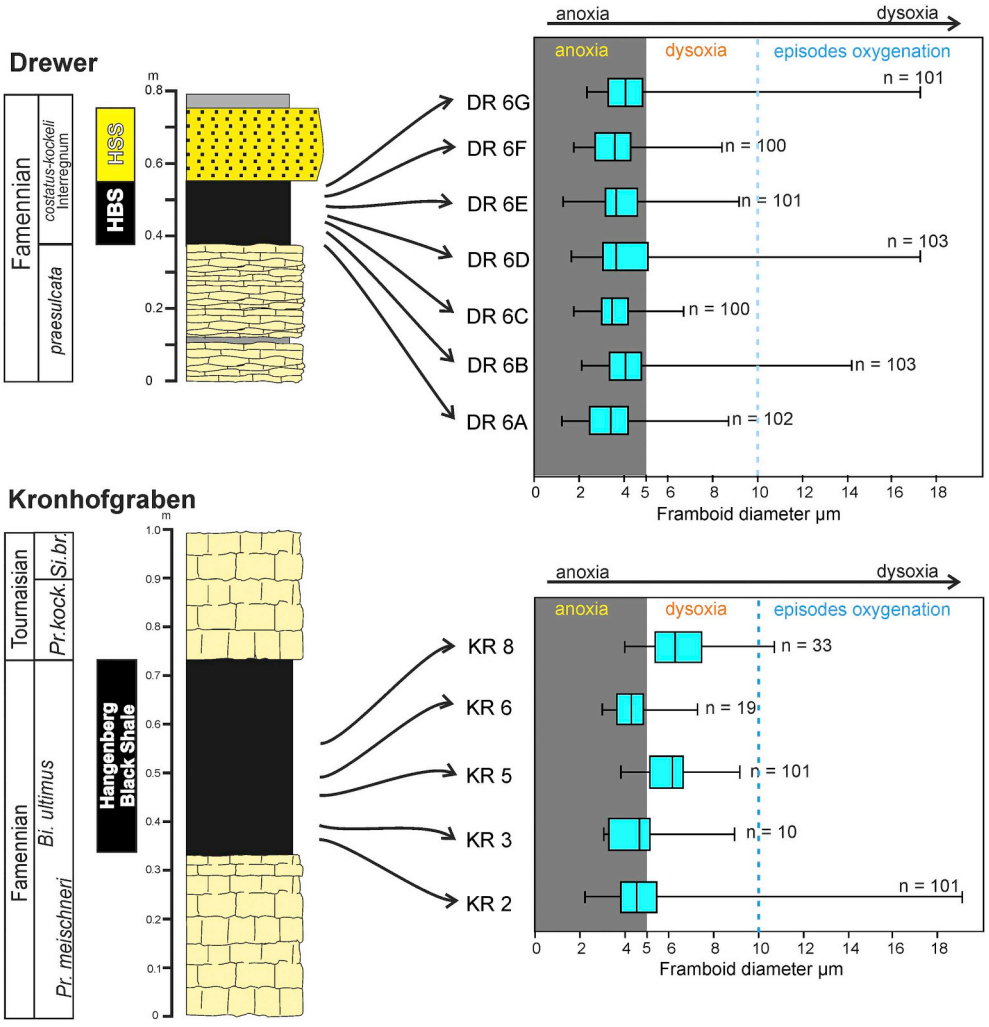

Fig. 9. Box and whisker plots with distribution of the pyrite framboids diameters across the HBS level at Krohofgraben (Carnic Alps) and Drewer (Rhenish Massif).

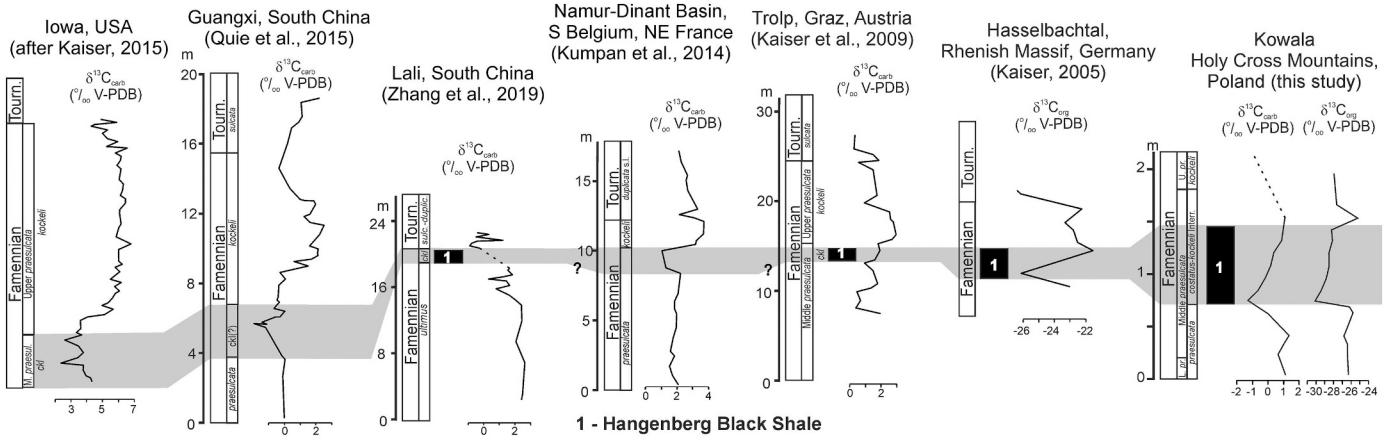

Fig. 10. Correlation based on carbon isotopes ($\delta^{13}C_{carb}$ and $\delta^{13}C_{org}$) of the top-Famennian sections in the North America, South China and Europe.

Al/(Al + Fe + Mn) values below 0.35 and Fe/Ti ratios above 20, and Al/(Al + Fe + Mn) values above 0.6 are indicative of an increase in the clay fraction supply to the basin (Boström, 1983; Dias and Barriga, 2006).

The higher values of Al/(Al + Fe + Mn) in the Carnic Alps, Rhenish Massif, Thuringia (Mn was below the detection limit, therefore we used 0.01 ppm as the Mn content for calculations) and the Holy Cross Mountains are generally above 0.6, and are thus indicative of an increased clay supply to the investigated basins (cf. Mouro et al., 2017; Rakociński et al., 2018), which is supported by mineralogical data: amount of phyllosilicates in the HBS is often above 50% (Table 2). Fe/Ti ratios are below 20 in almost all samples, which does not therefore confirm a hydrothermal influence. However, Kalvoda et al. (2018) noted low values of the Al/(Al + Fe + Mn) ratio in Moravian Karst from the Mokra quarry, which was interpreted as being hydrothermally influenced and probably related to Late Devonian rift magmatism in the eastern part of the Rhenohercynian zone.

In the Carnic Alps, the HBS interval is insignificantly enriched in Si, Ti, and Zr, which may reflect an increase of the coarser fraction and a subsequent increase in K. The latter may indicate an increased clay input (e.g., Turgeon and Brumsack, 2006). In the HBS interval of the Drewer section, enrichments in K and a depletion in Si, Zr, and Ti, reflect an increased input of muscovite and illitic illite–smectite (54–71%), and a subsequent decrease in coarser siliciclastics material. The exceptions are the Drewer and Hangenberg Sandstone units, which are characterized by enrichments in EF_{Zr}, EF_{Si}, and EF_{Ti} (Supplementary Data 3). In the Thuringia, increased Ti, Zr and K contents reflect an input of heavy minerals (anatase/rutile in range: 1.0 – 1.9%; and clay fraction; Table 2). At Kowala, the EF_{Ti} in the HBS interval is similar to that of an average shale composition, whereas EF_K and EF_{Zr} reflect distinctly enrichments in the HBS interval, and in background samples (Supplementary Data 3). This Zr enrichment is related to the delivery of zircon grains with a preserved euhedral shape whilst the increases of K content is related to the input of smectite and K-feldspar (sanidine).

The low Th/U ratios, high Mo and U concentrations, and the distribution and narrow sizes of pyrite framboids are all indicative of anoxic conditions in the water column. Th/U ratios in almost all investigated samples from the HBS have values < 3 (see Tables 3–7). Only one sample at Kowala quarry (KQ 110D) has a higher Th/U ratio (5.52), which may have been by increased detrital input of volcanogenic material (Marynowski et al., 2012; Table 6). V/Cr ratios > 4.25, which are typical for anoxic bottom conditions (cf. Jones and Manning, 1994;), were only determined for a number of samples from the Kowala (Table 8). The relationship between Cr and V is frequently used as a provenance proxy for the identification of ferromagnesian minerals and chromite (Bock et al., 1998). The presence of chromian spinels in the Drewer (Kołtonik et al., 2018) suggest that the V/Cr ratio in the studied sections may reflects the provenance of siliciclastic material rather than redox conditions (see criticism of the bi-metal proxies in Algeo and Liu, 2020). Elevated concentration of redox-sensitive elements such as Mo, U, V, Cu, and Ni, (Figs. 2–6; Tables 3–7), small diameter framboids (< 5 μm) with little variability in size, and high C_{org}/P ratios (> 150) indicate anoxic (even euxinic) conditions and higher productivity during HBS deposition in studied deep-water slope settings. The lack of simultaneous Co, Ni and Zn enrichments at Kahlleite may suggest that the HBS strata in the Saxo-Thuringia basin was deposited in the minimally sulfidic water conditions (Helz and Vorlicek, 2019).

According to Algeo and Tribovillard (2009) and Tribovillard et al. (2012), Mo and U covariation is useful for the reconstruction of ancient oceanic systems. The Mo_{EF} vs U_{EF} values in the HBS in the Kronhofgraben and Drewer (Fig. 11) are comparable to those from the upper Devonian Chattanooga Shale from the Appalachian Basin and parts of the Bakken Shale from the northern part of the Williston Basin, respectively. In the Kahlleite and Kowala sections, the Mo_{EF} vs U_{EF} values are similar to those of the Bakken Shale from the northern part of the Williston Basin (cf. fig. 8 in Algeo and Tribovillard, 2009; see data at Kowala in Marynowski et al., 2012), and are also comparable with modern analogues including the euxinic Cariaco Basin (Algeo and Tribovillard, 2009). The Cariaco Basin is a silled, deep basin with a weak restriction and rapid deep water renewal on the order of ~50–100 yr (Algeo and Lyons, 2006; Dahl et al., 2011). The deep water in this basin characterizes weakly euxinic marine conditions (Algeo and Tribovillard, 2009). The HBS sections from the Rhenohercynian (Drewer and Kowala) and Saxo-Thuringian (Kahlleite) basins may have also been weakly restricted basins, which were connected to the Rheic Ocean. In contrast, the Carnic Alps may have belonged to a subbasin within the “Plankogel ocean”, which would have been connected with the Paleo-Tethys Ocean (Läufer et al., 2001; Franke et al., 2017).

Appearance of the photic zone euxinia (PZE) was confirmed by specific biomarkers in the Kowala section (Marynowski et al., 2012). PZE probably occurred in other HBS sections, where a high maturity range did not allow for the measurement of biomarkers. Samples collected directly below the HBS in all sections were enriched in redox sensitive trace metals such as U, Mo, V, Cu, Pb, Cr, and Zn (with regionally small differences between enrichment or depletion of particular elements), which may imply that anoxic conditions started before facies changes and the initiation of sedimentation of the HBS. On the other hand, this could be related to the short-distance migration of pore-waters enriched in redox sensitive metals in the pore spaces through unlithified sediment during early diagenesis (e.g., Shaw et al., 1990).

Table 8
Evidence of volcanic and/or magmatic activity around the D/C boundary interval.

Locality	Reference
Ireland Munster Basin	Pracht (2000)
France Morvan region (French Massif Central)	Duthou et al. (1984)
Iberian Massif	González et al. (2006), Martínez Catalán et al. (2008)
Ukraine, southern part of Donbass fold belt, Pripyat-Dnieper-Donets rift	Wilson and Lyashkevlch (1996), McCann et al. (2003), Petrova (2010)
NW Russia and Karelia (Kola province)	Brown et al. (2006), Ricci et al. (2013), Arzamastsev et al. (2017)
East European Craton (Tajno and Ełk massifs)	Demaiffe et al. (2005), Krzemińska et al. (2006)
Eastern Siberia (Viluy LIP)	Ricci et al. (2013)
Southern Ural, Magnitogorsk Arc	Brown et al. (2006)
China (Daposhang in Guizhou Province).	Liu et al. (2012)
Czech Republic	Dvorak (1995), Kalvoda et al. (2018)
Germany, (Hasselbachtal in Rhenish Massif; Thuringia)	Korn and Weyer (2003), Trapp et al. (2004), Crônier (2007)
Poland (Holy Cross Mountains)	Marynowski et al. (2012), this study,
South Italy (Calabrian - Peloritan Arc)	Acquafredda et al. (1994)
Central North Sea (Embla Field)	Lundmark et al. (2012)
Atlantic Canada (Maritimes Basin)	Payette and Martin (1986), Dunning et al. (2002)
Portugal (South Portuguese Pyrite Belt)	Rosa et al. (2008)
Eastern Morocco (Anti-Atlas and western Meseta)	Pouclet et al. (2017)
Mongolia (Central Asian Orogenic Belt)	Wainwright et al. (2011)
North America, (Exshaw Formation; Yukon-Tanana Arc; Kootenay arc)	Richards and Higgins (1988), Dusen-Bacon and Williams (2009), Ward et al. (2019)
Central Asian Orogenic Belt	Wainwright et al., 2011
Australia (New England Belt)	Bryan et al. (2004)

8. Implications of geochemical and isotope data for the Hangenberg Crisis

8.1. Controls on the HBS deposition

One of the cause for the widespread deposition of the HBS and its equivalents in low-latitude shelf basins (Kaiser et al., 2006, 2015; Kumpan et al., 2015) may have been increased (or persisting) primary productivity in warming seawater temperatures (Kaiser et al., 2006; Simon et al., 2007). High productivity during deposition of the HBS interval may be expressed by the high content of amorphous organic matter and prasinophytes (Marynowski and Filipiak, 2007; Martinez et al., 2019), and the occurrence of numerous small gastropods at Kowala (see Marynowski et al., 2012, p. 70). Geochemical data in all the studied sections, as well as biomarker compositions suggest that permanent anoxic (to euxinic) bottom conditions prevailed during the early phase of HBS deposition in the Rhenohercynian basin and the part of Paleo-Tethys Ocean. The presence of green sulfur bacteria remains in the HBS in the Holy Cross Mountains (Marynowski and Filipiak, 2007; Marynowski et al., 2012) prove that euxinia reached the photic zone at least on a regional scale. Inorganic proxies suggest that the middle part of the HBS formed under intermittent bottom water anoxia or dysoxic conditions, with PZE in the water column. However, for example, in Kowala, the presence of laminated deposits, high TOC contents, the distribution and narrow size range of pyrite framboids that are typical for euxinic bottom conditions, and the highest content of clay minerals in the middle part of HBS all indicate the dilution effects by pyroclastic material rather than long-time changes of redox conditions. On the other hand, sporadic fossils of benthic organisms (in the Kowala section) and large framboids (> 10 μm in the Drewer and Kronhofgraben

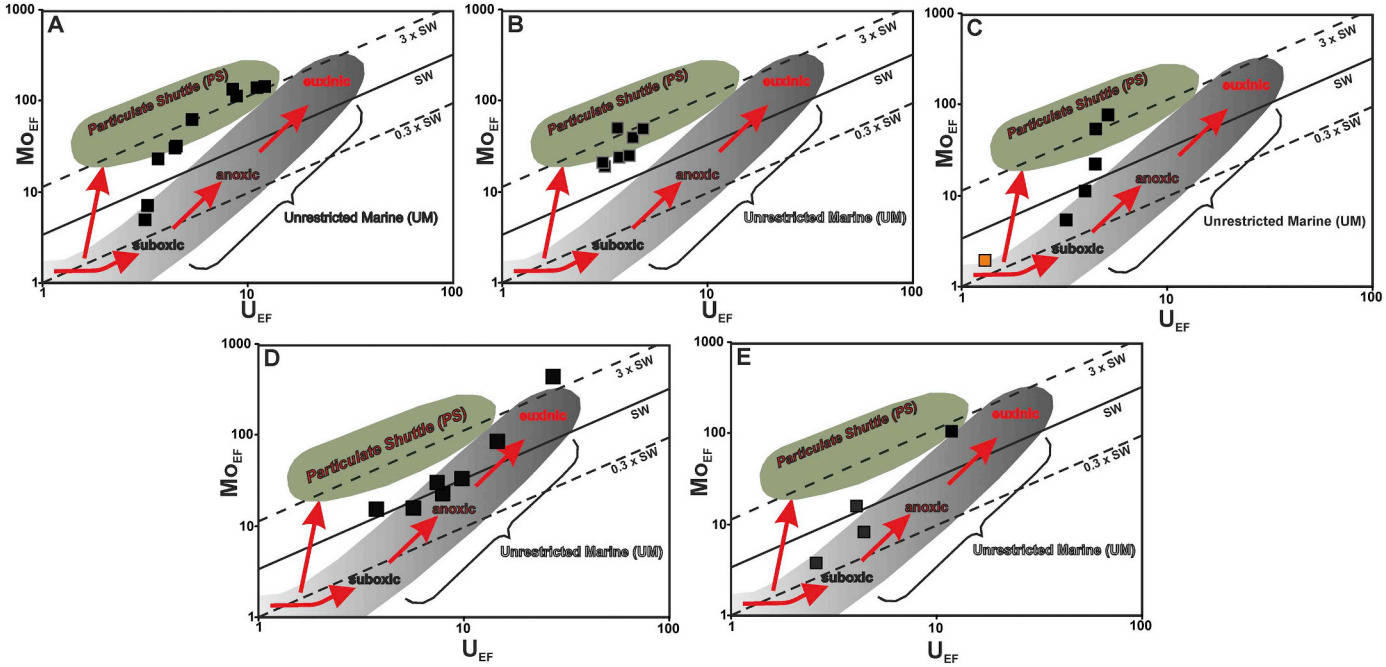

Fig. 11. Mo_{EF} versus U_{EF} for the HBS samples from Kronhofgraben (A), Drewer (B), Kahlleite (C), Kowala (D), and Plan di Zermula A (E). In the Kahlleite section the weathered sample is marked in orange.

sections) indicate that although the anoxic/euxinic bottom redox conditions prevailed during sedimentation of the HBS, episodes of short-term oxygenation of bottom waters and rapid colonization of the sea floor by opportunistic benthos had occurred (Marynowski et al., 2012; Martinez et al., 2019). The geochemical evidence of blooms of cyanobacteria, that are able to perform 2α-methylhopanoid biosynthesis, and chemotrophic organisms, suggests that these could have significantly changed the trophic structure of the open sea ecosystem. These blooms could therefore have had serious consequences for consumers of plankton and the higher food web (Kaiser et al., 2015).

Elevated influx of nutrient-rich terrigenous sediment has frequently been proposed as a cause of high primary productivity for Upper Devonian black shale deposition. In the opinion of some authors (e.g., Algeo and Scheckler, 1998), the spreading of land plants with deep root complexes during the greenhouse conditions at the end of the Devonian caused an increased continental weathering and a higher nutrient flux. Our study and previous observations in the studied areas (Bábek et al., 2016) revealed that a regional elevated continental influx could have stimulated primary productivity (e.g. in the Rhenish Massif). Retallack and Huang (2011; see also Lu et al., 2019) postulated that the expansion of large land-plants during short-lived CO_2-greenhouse spikes of warm and humid climates at the end of the Devonian were promoted, in part, by massive volcanic eruptions and/or meteorite impacts. Spikes in the pCO_2 could significantly enhance Mo accumulation (and lower $\delta^{98}Mo$) in mildly sulfidic conditions (Helz and Vorlicek, 2019). The elevated CO_2 that was consumed by spreading plants, enhanced silicate weathering on the land, and oceanic carbon sequestration resulted in the drawdown of atmospheric CO_2 and progressive cooling as it happened during the HBC (see fig. 2, Retallack and Huang, 2011; Kaiser et al., 2015). The globally reduced formation of carbonate during the Hangenberg Event interval could have also potentially lowered the pCO_2 of seawater (Ridgwell et al., 2003).

8.2. Magmatism as a trigger for the Hangenberg Crisis

Volcanic activity, exemplified by continental flood basalt eruptions in LIPs, can significantly raise atmospheric CO_2 concentrations and induce a catastrophic greenhouse effect (volcanic summer model of Wignall, 2005; see also Ernst, 2014; Racki, 2020b). Especially carbonatite alkaline magmatism (Ray and Pande, 1999), but also arc magmatism along continental-margin subduction zones (McKenzie et al., 2016; Lee et al., 2015), can release of catastrophic amounts of CO_2 into the atmosphere. On the other hand, submarine volcanic activity can be connected with phreatomagmatic eruptions and hydrothermal processes 'in the form of both water-rock exchange and magmatic degassing during eruptions of single large lava flows on the seafloor or subsurface dike injections' (Erba et al., 2015; p. 284). Svensen et al. (2018) showed that widespread sill intrusions and contact metamorphism with evaporites, carbonates, and organic-rich strata had a much deeper impact on CO_2 production than magma degassing alone. Volcanic activity is known to have occurred at the end of the Devonian (Fig. 12; Pracht and Batchelor, 1998; Trapp et al., 2004). The approximate age of 360 Ma is assumed as the end time in Siberian (Yakutsk–Vilyui) and East European LIPs (Ernst, 2014; Ernst et al., 2020), except for kimberlite intrusions (see summary in Racki, 2020a). Magmatic rocks and tuff layers exist in uppermost Devonian to Lower Carboniferous successions in many regions (Table 8, Fig. 12). Upper Devonian alkaline and/or carbonatite magmatic rocks are documented in northwest Russia and Karelia (Kola igneous province), and possibly occur also in the East European Craton (Tajno and Ełk massifs, with ages of 348 ± 15 Ma and 355 ± 4 Ma, respectively; Demaiffe et al., 2005; Krzemińska et al., 2006).

The existence of biotite (only in sample KQ 109A), sanidine and zircon grains with a preserved euhedral shapes and elevated smectitic I-S in the HBS samples and in a few layers underlying the HBS in the Kowala section, supports a volcanogenic origin of these minerals (bentonite, see Marynowski et al., 2012; Myrow et al., 2014). It is also supported by the K-Ar age of this biotite: 365 ± 10 Ma (M. Szczerba – unpublished results). The increase of Zr and K contents (Table 7) in the Kowala samples is probably indicative of increased explosive volcanism activity (see also Marynowski et al., 2012; Myrow et al., 2014) at the end of the Famennian stage. In the studied areas, pyroclastic horizons exist within the top-part of the Wocklum limestone in the Rhenish Massif (Hasselbachtal; Korn and Weyer, 2003; Trapp et al., 2004), and uppermost Famennian units of the Thuringia (Crônier, 2007; see Losau section in Racki, 2020a, fig. 18), Cracow Carbonate Platform (Czatkowice, Poland; M. Paszkowski – unpublished results) and radiolarian unit of the Bardo Mountains (Sudety, Poland; unpublished results). Kalvoda et al. (2019) detected volcanic rutile and titanite in the uppermost Famennian section in the Czech Republic (Bohemian Massif).

Volcanic activity and connected hydrothermal activity introduce large concentrations of some elements (mainly trace metals) that can be released in two modes: high-temperature, discrete magmatic degassing associated with single large eruptions, and low-temperature long-term water-rock reactions (Erba et al., 2015). Depending on which process dominated, different abundance patterns should occur. In the opinion of Rubin (1997), the high abundance of elements with shorter residence-times (e.g., Pb, Co, and Zn) may indicate which process of volcanic activity dominated, and provide an approximate source location.

EF patterns at four of the studied sites revealed contributions mainly from volatile elements (Fig. 13). The presence of these abundance peaks indicates that concentrations of elements in the basins at the studied sites were elevated by some mechanism other than fluxes of terrestrial runoff. Moreover, redox conditions at the sediment-water interface and an increased capture of elements by sinking organic particles cannot explain the entire variation in the trace element abundance.

8.2.1. Mercury as a proxy for magmatic activity

The recently successfully applied volcanic proxy Hg (see Clapham and Renne, 2019) exists in elevated concentrations (Figs. 2–6) at all sites. For Drewer, Kahlleite (Racki et al., 2018a) and Kowala strata, the Hg concentrations range from 0.13 to 0.28 ppm, 0.75 to 1.53 ppm, and 0.06 to 0.17 ppm, respectively. A very strong enrichment in Hg is present in the HBS at the Kronhofgraben (3.29–20.22 ppm) and Plan di Zermula A (1.35–9.76 ppm) sections. Hg deposition is primarily driven by complexation with organic matter (Sanei et al., 2012); hence, in almost all of the studied sections, Hg showed a strong positive correlation with the TOC content. Additionally, reducing (especially euxinic) conditions favor the incorporation of Hg into iron sulfides (Duan et al., 2016), but this process was generally insignificant in light of compiled data by Algeo and Liu (2020). A clear positive Hg/TOC spike only existed in Thuringia (Fig. 14), whereas there are anomalous Hg/TOC values in both Carnic Alps sections (> 71.9 ppb/wt%; Grasby et al., 2019, but compare with Charbonnier et al., 2020 and Racki, 2020a). Racki et al. (2018a) reported Hg anomalies around the D–C boundary from Uzbekistan. Paschall et al. (2019) described large enrichments in Hg (up to 1.09 ppm) and Hg/TOC anomalies in the HBS interval in the Pho Han Formation in the northeastern Vietnam (Fig. 14). Also, Kalvoda et al. (2019) found Hg and Hg/TOC spikes both within, below, and above the HBS in the Lesni Lom (Czech Republic) and Duli (Guangxi, China) sections (Fig. 14). In addition, Racki (2020a) recognized several different scale excursions of Hg and Hg/TOC in deep-water successions of Losau (Bavaria) and Shija (S-China), and highlighted their worldwide and euryfacies occurrence pattern, paired with local/regional imprint by hydrothermal processes. Due to the global occurrence of Hg anomalies, it is unlikely that redox conditions and/or clay input were the main effect on Hg patterns at the studied sites.

Dominant natural sources of Hg include effusive and explosive volcanism as well as explosive hydrothermal vent complexes that release gases generated by the contact metamorphism of organic-rich sediments (Pyle and Mather, 2003; Higueras et al., 2013). The largest

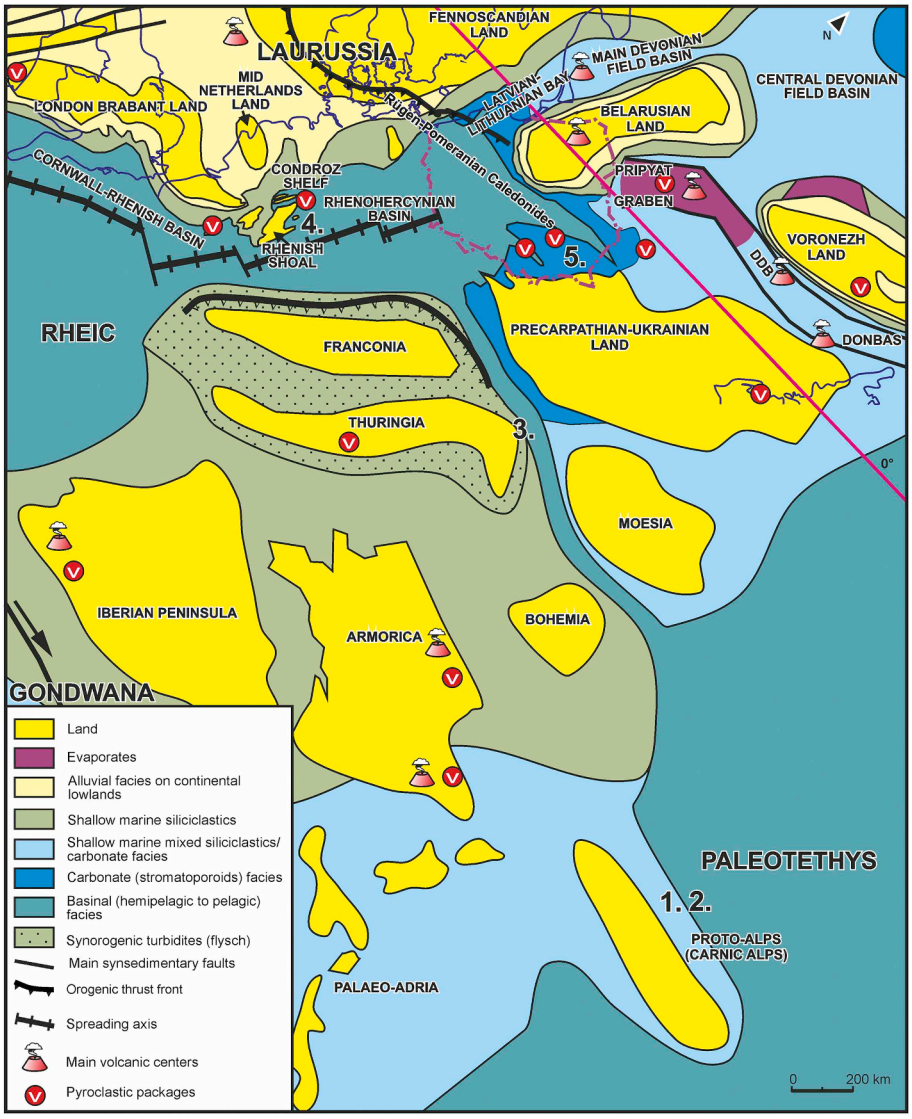

Fig. 12. Paleogeographic map of the top-Famennian magmatic and pyroclastic deposits in the vicinity of the studied areas. Presumed location of (1, 2) Kronhofgraben and Plan di Zermula A, (3) Kahlleite, (4) Drewer, (5) Kowala during the Hangenberg Crisis. Refer to Fig. 1; DDB - Dnieper-Donets basin. Location of volcanic and/or magmatic centers is presented in Table 8.

mercury ore formation known globally (Almadén, Spain) is linked to intraplate alkaline volcanism developed in submarine conditions connected with widespread hydrothermal activity during Silurian–Devonian time interval (Higueras et al., 2013). Hence, elevated Hg contents may indicate extensive volcanic activity (Percival et al., 2018, and references therein; Jones et al., 2019). Strong spatial variation in the Hg content may have resulted from variations in explosiveness and the style of volcanic eruptions. For example, marine (phreatomagmatic) eruptions may transfer part of the erupted Hg to seawater, thus resulting in a more limited global transport of this element (Percival et al., 2018; Jones et al., 2019). The mean ocean residence time of Hg has been estimated to range from 350 years (Gill and Fitzgerald, 1988) to 1 kyr (Matsunaga, 1981), and is shorter than the ocean mixing time of 1.5 kyr (Sarmiento and Gruber, 2006). Therefore, it can be expected that any Hg released into the water column will be redeposited at closer proximity to the source in comparison to atmospheric emissions (Rubin, 1997; Jones et al., 2019). Excluding post-depositional biases (Charbonnier et al., 2020), a great spatial variation in the magnitude of an Hg/TOC anomaly was explainable as a masking of the volcanic Hg signature by correlative increases in TOC (Percival et al., 2017; Racki, 2020a), a locality's proximity to a source (Jones et al., 2019) or interferences of different magmatic signals in episodes of tectono-magmatic activation (Racki, 2020a).

Enrichment in the more volatile trace metals at our studied settings may suggest the strong contribution of magmatic degassing during submarine eruptions. The high abundance of Hg in Kronhofgraben and Plan di Zermula A probably indicate a relatively close distance to the volcanic source of this element (as discussed by Jones et al., 2019). Because, there is no field evidence of volcanic activity near the Carnic microplate during the D/C boundary interval (the Raabtal metavolcanites and the volcanites of the Dimon Formation were deposited during early Carboniferous), the source of Hg could be back arc magmatic activity at the end of Famennian, whose traces were consumed during both Variscan and Alpine orogenesis.

The Hg anomaly in the uppermost Famennian strata of this study coincides with a negative $\delta^{13}C$ shift. A similar relationship between Hg enrichment, negative C-isotope excursions, volcanism, and anoxic events has been documented for the end of the Permian and Lower Triassic (Chen and Xu, 2019; Hammer et al., 2019; Schobben et al., 2019), terminal Triassic (Percival et al., 2017; Schobben et al., 2019), Pliensbachian–Toarcian boundary (Percival et al., 2015), lower Aptian (Charbonnier and Föllmi, 2017), and end of the Cretaceous (Percival

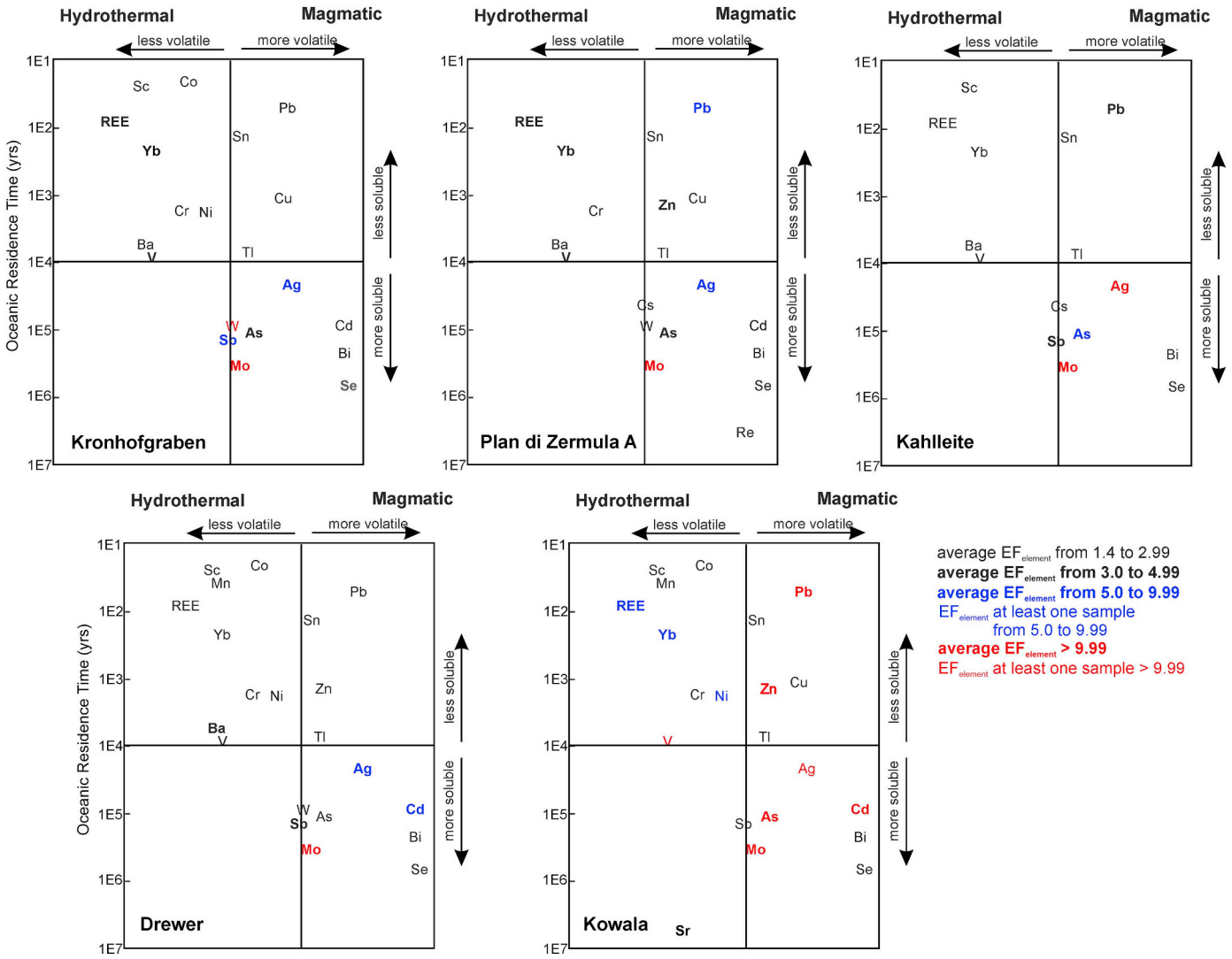

Fig. 13. The relative distribution of trace elements from the HBS interval into the gas phase released during the magmatic event and water-rock hydrothermal exchange reaction compared to the ocean residence times used to trace elements released during submarine volcanism (after Rubin, 1997).

et al., 2018). In addition, the Permian–Triassic C isotope event (P–Tr CIE) is attributed to both volcanogenic and thermogenic gas emissions from the Siberian Traps (Schobben et al., 2019). The intrusion of dikes into organic-rich strata, contemporary with volcanic activity, may have provided a source of additional ^{13}C-depleted carbon into the system.

8.2.2. *Possible volcanic contribution on the Hangenberg Crisis*

The existence of volcanic ash beds just below and within the HBS interval represents a potentially significant external nutrient driver of primary production ("ashfall events", Lee and Dee, 2019) and the eutrophication of ocean surface waters (Caplan et al., 1996), evidenced by very high organic matter content and elevated C_{org}/P values in the studied sections (see summary of volcanogenic fertilization in Racki, 2020b).

On the other hand, recent studies have shown that the negative effects of the dissolution of volcanic ash in seawater and magmatic degassing include the significant releases of toxic elements, e.g., Cu, Al, Hg and Se (Long et al., 2016), and acids leading to strong decreases in seawater pH (which is initially as low as pH 2.8 or 4; Jones and Gislason, 2008), and increased levels of toxicity. A seawater pH < 7.8 can cause an undersaturation of aragonite ($CaCO_3$) within a few meters of the water surface (Wall-Palmer et al., 2011). Acidification processes during the Hangenberg Event have been suggested, with the possible effects including the reduced calcification rates found at Kowala (this study and Marynowski et al., 2012), a temporary decrease in $CaCO_3$ contents observed in all of the studied samples (Figs. 2–5), and a mass mortality episode of marine plankton (Sallan and Coates, 2010; Lakin et al., 2016). Additionally, soot emission from volcanic-driven widespread fires (Marynowski and Filipiak, 2007) may have been an important trigger global changes (Tabor et al., 2020). The low abundance of the post-extinction recovery fauna, indicative of the Upper *praesulcata* Zone (Kumpan et al., 2015) may reflect the unfavorable conditions during this time; for example, a lack of available nutrients (see Jeppsson, 1990; Stricanne et al., 2006) or the delivery of Hg compounds that limited the development of biota (Rakociński et al., 2020). Additional evidence of a volcanic-inducted stress is the documented increase in the abundance of abnormal tetrads spores during the latest Famennian stage in the Holy Cross Mountains (Filipiak and Racki, 2010), in the Bardo Mountains (Matyja et al., 2020) and southern Belgium (Prestianni et al., 2016). A similar correlation between volcanic activity and the high occurrences of abnormal fern spores has been documented for the Permian–Triassic (Foster and Afonin, 2005; Fijałkowska-Mader, 2012) and the end-Triassic (Lindström et al., 2019) biotic crises.

The role of arc magmatism, which was extensive during the latest Devonian, is increasingly being emphasized as a trigger of global

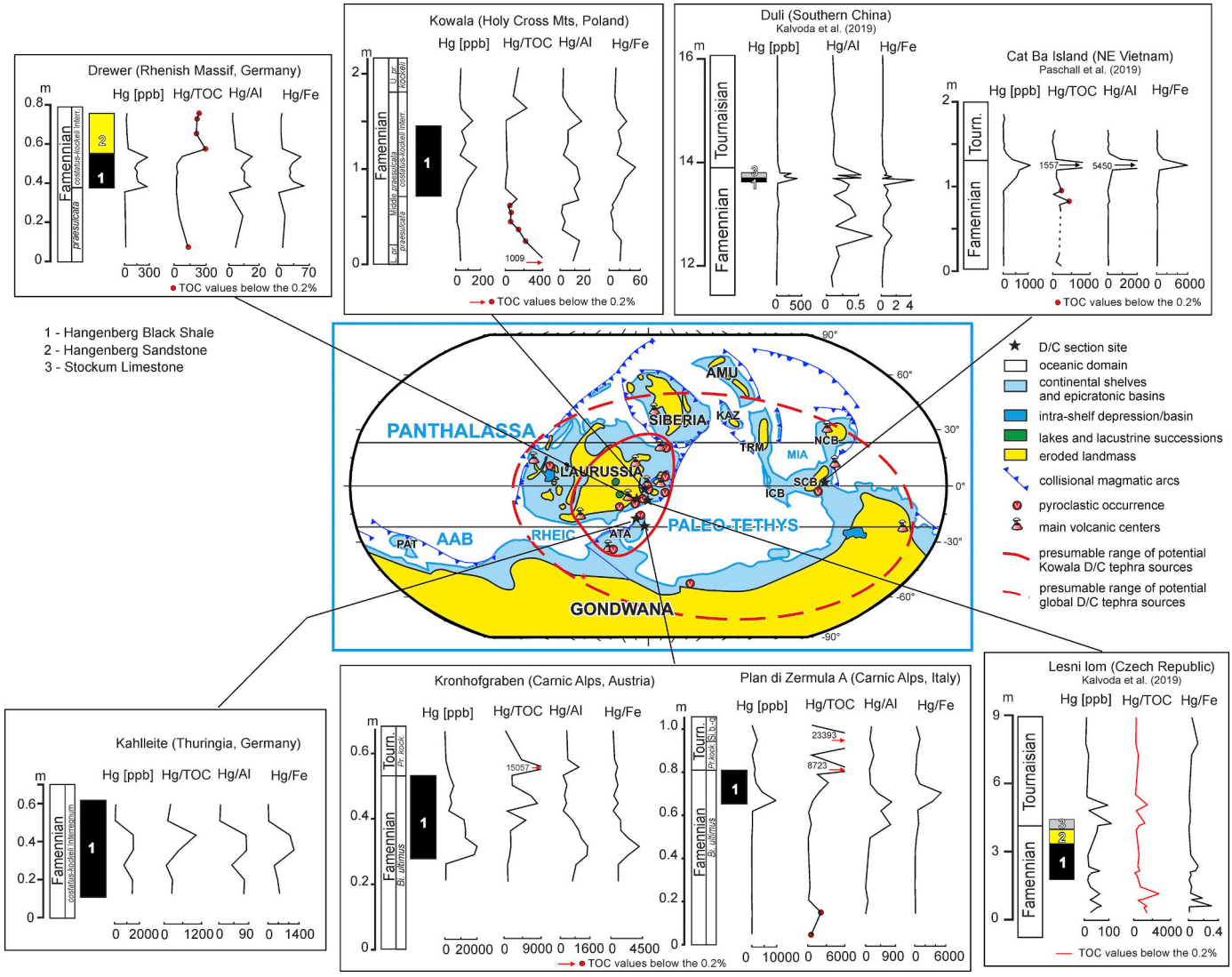

Fig. 14. Record of the Hg concentrations and Hg/TOC, Hg/Al and Hg/Fe ratios and global paleogeography with marked magmatic activity during the Devonian–Carboniferous boundary interval (for two additional sites in Germany and China see Racki, 2020a). The recommended limit for interpreting Hg/TOC concentrations is 0.2 wt% (Grasby et al., 2016). Red dots show Hg/TOC ratio for TOC values below 0.2%, generally pointing greater than potential Hg/TOC anomalies. Based on observations of recent and some ancient volcanic explosions, the distance between given location of tephra and most remote potential volcanic centers, as source for this tephra, depends on their type, but primarily on the size of the explosion. For example, for frequently occurring, small scale explosions, < 1 $km^3$of dispersed lava, it can be hundreds of kilometres (solid line circle), for sporadically occurring super volcanoes (> 1000 km^3) it can be many thousands of kilometres (dashed line). Global plate reconstructions after Young et al. (2019, modified). Abbreviation (blue, oceanic; yellow, continental): AAB, Arequipa-Antofalla Ocean, MIA, Mianlue Ocean; AMU, Amuria; KAZ, Kazakhstan; TRM, Tarim; NCB, North China; SCB, South China; ICB, Indochina; PAT, Patagonia.

environmental and biological changes (Sengör and Atayman, 2009; He et al., 2014; Lee et al., 2015; McKenzie et al., 2016). It must be remembered, however, that in order to preserve the Earth constant surface area, the increased activity of magmatic arcs must be balanced by the rifting and accretion of the new ocean floor. This type of marine magmatism does not generate more ashes, but significant amounts of volatile substances, including toxic gases and vapors, such as Hg, releasing directly into seawater. Rapid ocean floor spreading and growth of mid-oceanic ridge volume can also explain the Hangenberg transgression and related black shale deposition. The scale of this type of magmatism is likely underestimated due to almost complete subsequent destruction of Paleozoic oceanic crust (see e.g. Winter, 2015 for magmatism near the F–F boundary).

9. Conclusions

Outcrops of upper Famennian Hangenberg black shale (HBS) investigated in the present study were deposited in the deep part of the epeiric Rhenohercynian and Saxo–Thuringian basins, and in the more open sites of the Paleo-Tethys Ocean. Increased primary productivity during the HBS time interval is evidenced by very high organic matter content and elevated C_{org}/P values. Inorganic geochemical data (i.e., U/Th ratios, Mo concentrations and isotopes, and an enrichment in trace elements) and organic geochemical data (i.e., TOC and biomarkers), as well as framboid pyrite size distributions, indicate the development of predominantly anoxic/euxinic bottom-water conditions at all studied sites. In all of the studied sections, high Hg concentrations were detected, with the highest values found in the Carnic Alps (up to 20 ppm) and Thuringia (up to 1.5 ppm). The presence of both Hg anomaly and pyroclastic material below and within the HBS indicate that local magmatic activity was initiated before the deposition of the HBS. An enrichment in the more volatile trace metal in the studied sections may suggest a strong contribution of magmatic degassing during submarine eruptions, while the high abundance of Hg in the

Carnic Alps probably indicates that this site was in close proximity to the magmatic (?back arc) source of this element.

Anoxic bottom-water conditions in the studied deeper-water settings may have been caused by an enhanced phytoplankton productivity that could have been mainly related to arc magmatic activity. A negative organic carbon isotope excursion during the HBS was probably associated with increased photosynthetic C isotope fractionation under high $[CO_2]_{aq}$ conditions in the surface ocean above the chemocline, and elevated chemoautotrophic carbon fixation both at and below the chemocline.

Even if the major eruptive phases probably ended before the Hangenberg Crisis (HBC) in known continental LIPs (except for kimberlite explosions in Siberia), this cataclysmic activity could be spasmodically continued in the consumed oceanic LIPs (Kaiser et al., 2015), and/or thanks to the strongly enhanced arc magmatism, in combination with intensified seafloor eruptions in spreading zones and widespread hydrothermal venting (compare the F-F scenario in Racki, 2020a). Summarizing, a volcanically driven pulsed injection of catastrophic amounts of CO_2 could have led to greenhouse conditions and acidification during the HBC. Releases of toxic elements during the dissolution of volcanic ash in seawater and magmatic degassing may have resulted in mass mortality episodes of marine plankton and an increased abundance of abnormal tetrad spores.

For better understanding of the forcing mechanism of the HBC further research are required. The most relevant are (1) clarification of the ages of LIPs and carbonatite magmatism in the East European Craton to explain whether they could have triggered the HBC, (2) determination of the role of the "Bretonnian" tectonic activity in the latest Devonian, (3) explanation of the origin of the Hg peaks, and negative carbon excursions, and their spatiotemporal correlation. Moreover, (4) the oceanic acidification during the HBC requires comprehensive confirmation in the context of the present scenario.

Supplementary data to this article can be found online at https://doi.org/10.1016/j.gloplacha.2020.103155.

Declaration of competing interest

The authors declare that they have no known competing financial interests or personal relationships that could have appeared to influence the work reported in this paper.

Acknowledgements

Dieter Korn is acknowledged for his help in field works in the Rhenish Massif (in 2012). We thank Dorota Bakowska, Zuzanna Ciesielska, Beata Gebus-Czupyt, Marta Koziarska, Anna Mulczyk, Magdalena Radzikowska, Dariusz Sala, Anna Zagórska, Michał Zatoń and Małgorzata Zielińska for their laboratory assistance. Andrzej Łaptaś assisted with the drawing of Figs. 1B, 12, and 14. This study was supported by the National Science Centre in Poland research grants 2011/03/B/ST10/04602, 2013/08/A/ST10/00717 and 2014/15/B/ST10/03705. The paper was greatly improved following suggestions by Paul Myrow, an anonymous reviewer, and by guest editor Paul Wignall.

References

Acquafredda, P., Lorenzoni, S., Lorenzoniet, E.Z., 1994. Palaeozoic sequences and evolution of the Calabrian-Peloritan Arc (Southern Italy). Terra Nova 6, 582–594.

Algeo, T.J., Liu, J., 2020. A re-assessment of elemental proxies for paleoredox analysis. Chem. Geol. https://doi.org/10.1016/j.chemgeo.2020.119549. (in press).

Algeo, T.J., Lyons, T.W., 2006. Mo-total organic carbon covariation in modern anoxic marine environments: implications for analysis of paleoredox and paleohydrographic conditions. Paleoceanography 21, PA1016.

Algeo, T.J., Scheckler, S.E., 1998. Terrestrial–marine teleconnections in the Devonian; links between the evolution of land plants, weathering processes, and marine anoxic events. R. Soc. Lond. Philos. Trans. 353, 113–130.

Algeo, T.J., Tribovillard, N., 2009. Environmental analysis of paleoceanographic systems based on molybdenum–uranium covariation. Chem. Geol. 268, 211–225.

Anbar, A.D., Knab, K.A., Barling, J., 2001. Precise determination of mass-dependent variations in the isotopic composition of molybdenum using MC-ICPMS. Anal. Chem. 73, 1425–1431.

Arnold, G.L., Anbar, A.D., Barling, J., Lyons, T.W., 2004. Molybdenum isotope evidence for widespread anoxia in mid-Proterozoic oceans. Science 304, 87–90.

Arthur, M.A., Dean, W.E., Claypool, G.E., 1985. Anomalous ^{13}C enrichment in modern marine organic carbon. Nature 315, 216–218.

Arzamastsev, A.A., Vesolovskiyc, R.V., Travine, A.V., Yudine, D.S., Belyatskyh, B.V., 2017. Paleozoic tholeiitic magmatism of the kola province: spatial distribution, age, and relation to alkaline magmatism. Petrology 25, 42–65.

Asael, D., Tissot, F.L.H., Reinhard, C.T., Rouxel, O., Dauphas, N., Lyons, T.W., Ponzevera, E., Liorzou, C., Chéron, S., 2013. Coupled molybdenum, iron and uranium stable isotopes as oceanic paleoredox proxies during the Paleoproterozoic Shunga Event. Chem. Geol. 362, 193–210.

Bábek, O., Kumpan, T., Kalvoda, J., Matys Grygar, T., 2016. Devonian/Carboniferous boundary glacioeustatic fluctuations in a platform-to-basin direction: a geochemical approach of sequence stratigraphy in pelagic settings. Sediment. Geol. 337, 81–99.

Barling, J., Arnold, G.L., Anbar, A.D., 2001. Natural mass-dependent variations in the isotopic composition of molybdenum. Earth Planet. Sci. Lett. 193, 447–457.

Becker, R.T., Hartenfels, S., Weyer, D., Kumpan, T., 2016. The Famennian to Lower Viean at Drewer (northern Rhenish Massif). Münstersche Forsch. Geol. Paläont. 108, 158–178.

Beerling, D.J., Lomax, B.H., Royer, D.L., Upchurch, G.R.J., Kump, L.R., 2002. An atmospheric pCO2 reconstruction across the Cretaceous–Tertiary boundary from leaf megafossils. Proc. Natl. Acad. Sci. 99, 7836–7840.

Berkowski, B., 2002. Famennian Rugosa and Heterocorallia from Southern Poland. Palaeontol. Pol. 61, 3–88.

Blakey, R., 2016. Devonian - 360 Ma, Global Paleogeography and Tectonics in Deep Time Series. Deep Time Maps™ Paleogeography.

Bock, B., McLennan, S.M., Hanson, G.N., 1998. Geochemistry and provenance of the Middle Ordovician Austin Glen Member (Normanskill Formation) and the Taconian orogeny in New England. Sedimentology 45, 635–655.

Bojar, A.-V., Neubauer, F., Koeberl, C., 2013. Geochemical record of Late Devonian to early carboniferous events, palaeozoic of graz, eastern alps, Austria. Geol. Soc. Lond., Spec. Publ. 376, 87–108.

Bond, D., Wignall, P.B., Racki, G., 2004. Extent and duration of marine anoxia during the Frasnian–Famennian (Late Devonian) mass extinction in Poland, Germany, Austria and France. Geol. Mag. 141, 173–193.

Boström, K., 1983. Genesis of ferromanganese deposits – diagnostic criteria for recent and old deposits. In: Rona, P.A., Boström, K., Laubier, L., Smith, K.L. (Eds.), Hydrothermal Processes at Seafloor Spreading Centers. Plenum Press, New York, pp. 473–483.

Brand, U., Legrand-Blain, M., Streel, M., 2004. Biochemostratigraphy of the Devonian – Carboniferous boundary global stratotype section and point, Griotte Formation, La Serre, Montagne Noire, France. Palaeogeogr. Palaeoclimatol. Palaeoecol. 205 (3–4), 337–357.

Brown, D., Spadea, P., Puchkov, V., Alvarez-Marron, J., Herrington, R., Willner, A.P., Hetzel, R., Gorozhanina, Y., Juhlin, C., 2006. Arc-continent collision in the Southern Urals. Earth Sci. Rev. 79, 261–287.

Brumsack, H.-J., 2006. The trace metal content of recent organic carbon-rich sediments: implications for Cretaceous black shale formation. Palaeogeogr. Palaeoclimatol. Palaeoecol. 232, 344–361.

Brüske, A., Weyer, S., Zhao, M.-Y., Planavsky, N.J., Wegwerth, A., Neubert, N., Dellwig, O., Lau, K.V., Lyons, T.W., 2020. Correlated molybdenum and uranium isotope signatures in modern anoxic sediments: implications for their use as paleo-redox proxy. Geochim. Cosmochim. Acta 270, 449–474.

Bryan, S.E., Allen, C.M., Holcombe, R.J., Fielding, C.R., 2004. U–Pb zircon geochronology of Late Devonian to Early Carboniferous extension-related silicic volcanism in the northern New England Fold Belt. Aust. J. Earth Sci. 51, 645–664.

Buggisch, W., Joachimski, M.M., 2006. Carbon isotope stratigraphy of the Devonian of central and southern Europe. Palaeogeogr. Palaeoclimatol. Palaeoecol. 240, 66–88.

Calvert, S.E., Pedersen, T.F., 2007. Chapter fourteen elemental proxies for palaeoclimatic and palaeoceanographic variability in marine sediments: interpretation and application. Dev. Mar. Geol. 113, 67–88. https://doi.org/10.1016/S15725480(07)01019-6.

Caplan, M.L., Bustin, R.M., 1999. Devonian–Carboniferous Hangenberg mass extinction event, widespread organic-rich mudrock and anoxia: causes and consequences. Palaeogeogr. Palaeoclimatol. Palaeoecol. 148, 187–207.

Caplan, M.L., Bustin, R.M., Grimm, K.A., 1996. Demise of a Devonian–Carboniferous carbonate ramp by eutrophication. Geology 24, 715–718.

Carmichael, S.K., Waters, J.A., Batchelor, C.J., Coleman, D.M., Suttner, T.J., Kido, E., Moore, L.M., Chadimová, L., 2016. Climate instability and tipping points in the Late Devonian: detection of the Hangenberg event in an open oceanic island arc in the Central Asian Orogenic Belt. Gondwana Res. 32, 213–231.

Charbonnier, G., Föllmi, K.B., 2017. Mercury enrichments in lower Aptian sediments support the link between Ontong Java large igneous province activity and oceanic anoxic episode 1a. Geology 45, 63–66.

Charbonnier, G., Adatte, T., Föllmi, K.B., Suan, G., 2020. Effect of intense weathering and post-depositional degradation of organic matter on Hg/TOC proxy in organic-rich sediments and its implications for deep-time investigations. Geochem. Geophys. Geosyst. 21 e2019GC008707.

Chen, J., Xu, Y., 2019. Establishing the link between Permian volcanism and biodiversity changes: insights from geochemical proxies. Gondwana Res. 75, 68–96.

Clapham, M.E., Renne, P.R., 2019. Flood basalts and mass extinctions. Annu. Rev Earth Planet. Sc. 47, 275–303.

Conway, N.M., Kennicutt, M.C., Van Dover, C.L., 1994. Stable isotopes in the study of marine chemosynthetic-based food webs. In: Lajtha, K., Michener, R. (Eds.), Stable

Isotopes in Ecology and Environmental Science. Blackwell Scientific Publications, Oxford, pp. 158–186.
Corradini, C., Spalletta, C., Mossoni, A., Matyja, H., Over, D.J., 2017. Conodonts across the Devonian/Carboniferous boundary: a review and implication for the redefinition of the boundary and a proposal for an updated conodont zonation. Geol. Mag. 154 (4), 888–982. Cambridge University Press 2016. https://doi.org/10.1017/S001675681600039X.
Courtillot, V., Renne, P.R., 2003. On the ages of flood basalt events. Compt. Rendus Geosci. 335, 113–140.
Cramer, B., Saltzman, M., Day, J.E., Witzke, B.J., 2008. Record of the Late Devonian Hangenberg global positive carbon-isotope excursion in an epeiric sea setting: carbonate production, organic-carbon burial and paleoceanography during the Late Famennian. Dyn. Epeiric Seas. Geol. Assoc. Can. Spec. Pap. 48, 103–118.
Creaser, R.A., Sannigrahi, P., Chacko, T., Selby, D., 2002. Further evaluation of the Re–Os geochronometer in organic-rich sedimentary rocks: a test of hydrocarbon maturation effects in the Exshaw Formation, Western Canada Sedimentary Basin. Geochim. Cosmochim. Acta 66, 3441–3452.
Crônier, C., 2007. Larval morphology and ontogeny of an Upper Devonian phacopid: Nephranops from Thuringia, Germany. J. Paleontol. 81, 684–700.
Dahl, T.W., Hammarlund, E.U., Anbar, A.D., Bond, D.P.G., Gill, B.C., Gordon, G.W., Knoll, A.H., Nielsen, A.T., Schovsbo, N.H., Canfield, D.E., 2010. Devonian rise in atmospheric oxygen correlated to the radiations of terrestrial plants and large predatory fish. PNAS 107, 17911–17915.
Dahl, T.W., Canfield, D.E., Rosing, M.T., Frei, R.E., Gordon, G.W., Knoll, A.H., Anbar, A.D., 2011. Molybdenum evidence for expansive sulfidic water masses in similar to 750 Ma oceans. Earth Planet. Sci. Lett. 311, 264–274.
Day, J., Witzke, B.J., Rowe, H., Elwood, B., 2013. Magnetic susceptibility and carbon isotope stratigraphies through the Devonian-Carboniferous boundary interval in the western Illinois basin – central North America. In: Whalen, M., Osadetz, K., Richards, B., Kabanov, P., Weissenberger, J., Potma, K., Koenigshof, P., Suttner, T., Kido, E., Da Silva, A.-C. (Eds.), Geophysical and Geochemical Techniques: A Window on the Palaeozoic World, IGCP 580–596, 27 August – 1 September 2013, Programme with Abstracts.
De Vleeschouwer, D., Rakociński, M., Racki, G., Bond, D.P., Sobień, K., Claeys, P., 2013. The astronomical rhythm of Late-Devonian climate change (Kowala section, Holy Cross Mountains, Poland). Earth Planet. Sci. Lett. 365, 25–37.
Demaiffe, D., Wiszniewska, J., Brassinnes, S., 2005. A petrological–geochemical overview of the Tajno carbonatite complex (NE Poland). Comparison with the Kola Carbonatite Province (Russia). Pr. Specjalne PTM 26, 29–35.
Derkowski, A., Marynowski, L., 2018. Binding of heavy metals by oxidised kerogen in (palaeo)weathered black shales. Chem. Geol. 493, 441–450.
Dias, A.S., Barriga, F.J.A.S., 2006. Mineralogy and geochemistry of hydrothermal sediments from the serpentinite-hosted Saldanha hydrothermal field (36°34′N; 33°26′W) at MAR. Mar. Geol. 225, 157–175.
Dickens, G.R., O'Neil, J.R., Rea, D.K., Owen, R.M., 1995. Dissociation of oceanic methane hydrate as a cause of the carbon isotope excursion at the end of the Paleocene. Paleoceanography 10 (6), 965–971.
Duan, Y., Anbar, A.D., Arnold, G.L., Lyons, T.W., Gordon, G.W., Kendall, B., 2010. Molybdenum isotope evidence for mild environmental oxygenation before the Great Oxidation Event. Geochim. Cosmochim. Acta 74, 6655–6668.
Duan, Y., Han, D.S., Batchelor, B., Abdel-Wahab, A., 2016. Synthesis, characterization, and application of pyrite for removal of mercury. Colloids Surf. A Physicochem. Eng. Asp. 490, 326–335.
Dunning, G.R., Barr, S.M., Giles, P.S., McGregor, D.C., Pe-Piper, G., Piper, D.J.W., 2002. Chronology of Devonian to early Carboniferous rifting and igneous activity in southern Magdalen Basin based on U-Pb (zircon) dating. Can. J. Earth Sci. 39, 1219–1237.
Dusen-Bacon, C., Williams, I.S., 2009. Evidence for prolonged mid-Paleozoic plutonism and ages of crustal sources in east-central Alaska from SHRIMP U-Pb dating of syn-magmatic, inherited, and detrital zirocn. Can. J. Earth Sci. 46, 21–39.
Duthou, J.L., Cantagrel, J.M., Didier, J., Vialette, Y., 1984. Palaeozoic granitoids from the French Massif Central: age and origin studied by ^{87}Rb-^{87}Sr system. Phys. Earth Planet. Inter. 35, 131–144.
Dvorak, J., 1995. Stratigraphy. In: Dallmeyer, R.D., Franke, W., Weber, K. (Eds.), Pre-Permian Geology of Central and Eastern Europe. Springer, Berlin, Heidelberg, pp. 477–489.
Erba, E., Duncan, R.A., Bottini, C., Tiraboschi, D., Weissert, H., Jenkyns, H.C., Malinverno, A., 2015. Environmental consequences of Ontong Java Plateau and Kerguelen Plateau volcanism. In: Neal, C.R., Sager, W.W., Sano, T., Erba, E. (Eds.), The Origin, Evolution, and Environmental Impact of Oceanic Large Igneous Provinces. Geological Society of America Special Paper 511. pp. 271–303. https://doi.org/10.1130/2015.2511(15).
Ernst, R.E., 2014. Large Igneous Provinces. Cambridge University Press 653 pp.
Ernst, R.E., Rodygin, S.A., Grinev, O.M., 2020. Age correlation of Large Igneous Provinces with Devonian biotic crises. Glob. Planet. Chang. 185 (103097).
Fijałkowska-Mader, A., 2012. Odzwierciedlenie stresu środowiskowego w palinoflorze późnego permu w Polsce. Biul. Państwowego Inst. Geol. 452, 23–32.
Filipiak, P., Racki, G., 2010. Proliferation of abnormal palynoflora during the end-Devonian biotic crisis. Geol. Q. 54, 1–14.
Forster, A., Culshaw, M.G., Bell, F.G., 1995. Regional distribution of sulphate in rocks and soils of Britain. Geol. Soc. Lon., Eng. Geol. Spec. Publ. 10, 95–104.
Franke, W., Eder, W., Engel, W., Langenstrassen, F., 1978. Main aspects of geosynclinal sedimentation in the Rhenohercynian Zone. Z. Dtsch. Geol. Ges. 129 (1), 201–216.
Foster, C.B., Afonin, S.A., 2005. Abnormal pollen grains: an outcome of deteriorating atmospheric conditions around the Permian–Triassic boundary. J. Geol. Soc. Lond. 162, 653–659.
Franke, W., Cocks, L.R.M., Torsvik, T.H., 2017. The Palaeozoic Variscan oceans revisited. Gondwana Res. 48, 257–284.
Frisch, W., Neubauer, F., 1989. Pre-Alpine terranes and tectonic zoning in the eastern Alps. Geol. Soc. Am. Spec. Pap. 230, 91–100.
Gereke, M., 2004. Das Profil Kahlleite Ost - die stratigraphische Entwicklung einer Tiefschwelle im Oberdevon des Bergaer Sattels (Thüringen). Geol. Palaeontol. 38, 1–31.
Gereke, M., 2007. Die oberdevonische Kellwasser-Krise in der Beckenfazies von Rhenoherzynikum und Saxothuringikum (spätes Frasnium/frühestes Famennium. Deutschland). Kölner Forum Geol. Paläontol. 17, 1–228.
Gill, G.A., Fitzgerald, W.F., 1988. Vertical mercury distributions in the oceans. Geochim. Cosmochim. Acta 52, 1719–1728.
Goldberg, T., Archer, C., Vance, D., Poulton, S.W., 2009. Mo isotope fractionation during adsorption to Fe (oxyhydr)oxides. Geochim. Cosmochim. Acta 73, 6502–6516.
Goldberg, T., Gordon, G., Izon, G., Archer, C., Pearce, C.R., McManus, J., Anbar, A.D., Rehkämper, M., 2013. Resolution of inter-laboratory discrepancies in Mo isotope data: an intercalibration. J. Anal. At. Spectrom. 28, 724–735.
González, F., Moreno, C., Santos, A., 2006. The massive sulphide event in the Iberian Pyrite Belt: confirmatory evidence from the Sotiel-Coronada Mine. Geol. Mag. 143 (6), 821–827.
Gordon, G.W., Lyons, T.W., Arnold, G.L., Roe, J., Sageman, B.B., Anbar, A.D., 2009. When do black shales tell Mo isotope tales? Geology 37, 535–538.
Grasby, S., Beauchamp, B., Bond, D., Wignall, P., Sanei, H., 2016. Mercury anomalies associated with three extinction events (Capitanian Crisis, Latest Permian Extrinction and the Smithian/Spathian Extinction) in NW Pangea. Geol. Mag. 153, 285–297.
Grasby, S.E., Them, Chen, Z., Yin, R.S., Ardakani, O.H., 2019. Mercury as a proxy for volcanic emissions in the geologic record. Earth-Sci. Rev. 196, 102880.
Hammer, Ø., Jones, M.T., Schneebeli-Hermann, E., Hansen, B.B., Bucher, H., 2019. Are Early Triassic extinction events associated with mercury anomalies? A reassessment of the Smithian/Spathian boundary extinction. Earth Sci. Rev. 195, 179–190.
He, B., Zhong, Y.T., Xu, Y.G., Li, X.H., 2014. Triggers of Permo-Triassic boundary mass extinction in South China: the Siberian Traps or Paleo-Tethys ignimbrite flare-up? Lithos 204, 258–267.
Helz, G.R., Vorlicek, T.P., 2019. Precipitation of molybdenum from euxinic waters and the role of organic matter. Chem. Geol. 509, 178–193.
Higueras, P., Oyarzun, R., Lillo, J., Morata, D., 2013. Intraplate mafic magmatism, degasification, and deposition of mercury: the giant Almadén mercury deposit (Spain) revisited. Ore Geol. Rev. 51, 93–102.
Hollander, D.J., Smith, M.A., 2001. Microbially mediated carbon cycling as a control on the ^{13}C of sedimentary carbon in eutrophic Lake Mendota (USA): new models for interpreting isotopic excursions in the sedimentary record. Geochim. Cosmochim. Acta 65, 4321–4337.
Jahren, A.H., 2002. The biogeochemical consequences of the mid-Cretaceous superplume. J. Geodyn. 34, 177–191.
Jeppsson, L., 1990. An oceanic model for lithological and faunal changes tested on the Silurian record. J. Geol. Soc. Lond. 147, 663–674.
Jones, M.T., Gislason, S.R., 2008. Rapid releases of metal salts and nutrients following the deposition of volcanic ash into aqueous environments. Geochim. Cosmochim. Acta 72, 3661–3680.
Jones, B., Manning, D.A., 1994. Comparison of geochemical indicates used for the interpretation of palaeoredox conditions in ancient mudstones. Chem. Geol. 111, 111–129.
Jones, M.T., Jerram, D.A., Svensen, H.H., Grove, C., 2016. The effects of large igneous provinces on the global carbon and sulphur cycles. Palaeogeogr. Palaeoclimatol. Palaeoecol. 441, 4–21.
Jones, M.T., Percival, L.M.E., Stokke, E.W., Frieling, J., Mather, T.A., Riber, L., Schubert, B.A., Schultz, B., Tegner, C., Planke, S., Svensen, H.H., 2019. Mercury anomalies across the Palaeocene–Eocene thermal maximum. Clim. Past 15, 217–236. https://doi.org/10.5194/cp-15-217-2019.
Kaiser, S., 2005. Mass Extinctions, Climatic and Oceanographic Changes at the Devonian/Carboniferous Boundary. unpublished PhD Thesis, Ruhr-Universität, Bochum, Germany, 160 p.
Kaiser, S.I., Steuber, T., Becker, R.T., Joachimski, M.M., 2006. Geochemical evidence for major environmental change at the Devonian–Carboniferous boundary in the Carnic Alps and the Rhenish Massif. Palaeogeogr. Palaeoclimatol. Palaeoecol. 240, 146–160.
Kaiser, S.I., Steuber, T., Becker, R.T., 2008. Environmental change during the Late Famennian and Early Tournaisian (Late Devonian–Early Carboniferous): implications from stable isotopes and conodont biofacies in southern Europe. Geol. J. 43, 241–260.
Kaiser, S.I., Becker, R.T., Spalletta, C., Steuber, T., 2009. High-resolution conodont stratigraphy, biofacies, and extinctions around the Hangenberg Event in pelagic successions from Austria, Italy, and France. Palaeontogr. Am. 63, 99–143.
Kaiser, S.I., Becker, R.T., Steuber, T., Aboussalam, S.Z., 2011. Climate-controlled mass extinctions, facies, and sea-level changes around the Devonian–Carboniferous boundary in the eastern Anti-Atlas (SE Morocco). Palaeogeogr. Palaeoclimatol. Palaeoecol. 310, 340–364.
Kaiser, S.I., Aretz, M., Becker, R.T., 2015. The global Hangenberg Crisis (Devonian–Carboniferous transition): review of a first-order mass extinction. In: Becker, R.T., Königshof, P., Brett, C.E. (Eds.), Devonian Climate, Sea Level and Evolutionary Events. Geological Society of London Special Publication 423. pp. 387–437.
Kalvoda, J., Kumpan, T., Holá, M., Bábek, O., Kanický, V., Škoda, R., 2018. Fine-scale LA-ICP-MS study of redox oscillations and REEY cycling during the latest Devonian Hangenberg Crisis (Moravian Karst, Czech Republic). Palaeogeogr. Palaeoclimatol. Palaeoecol. 493, 30–43.
Kalvoda, J., Kumpan, T., Qie, W., Frýda, J., Bábek, O., 2019. Mercury spikes at the

Devonian-Carboniferous boundary in the eastern part of the Rhenohercynian zone (central Europe) and in the South China block. Palaeogeogr. Palaeoclimatol. Palaeoecol. https://doi.org/10.1016/j.palaeo.2019.05.043.
Kazmierczak, J., Kremer, B., Racki, G., 2012. Late Devonian marine anoxia challenged by benthic cyanobacterial mats. Geobiology 10, 371–383.
Kendall, B., Gordon, G.W., Poulton, S.W., Anbar, A.D., 2011. Molybdenum isotope constraints on the extent of late Paleoproterozoic ocean euxinia. Earth Planet. Sci. Lett. 307, 450–460.
Klein, C., 2016. Testing Modern Biostratigraphical Methods. Springer Spectrum, Berlin.
Kołtonik, K., Pisarzowska, A., Paszkowski, M., Sláma, J., Becker, R.T., Szczerba, M., Krawczyński, W., Hartenfels, S., Marynowski, L., 2018. Baltic provenance of top-Famennian siliciclastic material of the northern Rhenish Massif, Rhenohercynian zone of the Variscan orogen. Int. J. Earth Sci. 107, 2645–2669.
Kołtonik, K., Pisarzowska, A., Paszkowski, M., Sláma, J., Becker, R.T., Szczerba, M., Krawczyński, W., Hartenfels, S., Marynowski, L., Mazur, S., Franke, W., 2019. Reply to Comment by M.F. Pereira, J.B. Silva and C. Gama on "Baltic provenance of top-Famennian siliciclastic material of the northern Rhenish Massif, Rhenohercynian zone of the Variscan orogen, by Koltonik et al., International Journal of Earth Sciences (2018) 107: 2645-2669". Int. J. Earth Sci. 108, 1075–1078.
Komatsu, T., Kato, S., Hirata, K., Takashima, R., Ogata, Y., Oba, M., Naruse, H., Ta, P.H., Nguyen, P.D., Dang, H.T., 2014. Devonian–Carboniferous transition containing a Hangenberg Black Shale equivalent in the Pho Han Formation on Cat Ba Island, northeastern Vietnam. Palaeogeogr. Palaeoclimatol. Palaeoecol. 404, 30–43.
Königshof, P., Savage, N.M., Lutat, P., Sardsud, A., Dopieralska, J., Belka, Z., Racki, G., 2012. Late Devonian sedimentary record of the Paleotethys Ocean — the Mae Sariang section, northwestern Thailand. J. Asian Earth Sci. 52, 146–157. https://doi.org/10.1016/j.jseaes.2012.03.006.
Königshof, P., Becker, R.T., Hartenfels, S., 2016. The Rhenish Massif as a part of the European Variscides. Münstersche Forsch. Geol. Palaeontol. 108, 1–13.
Koopmans, M.P., Schouten, S., Kohnen, M.E.L., Sinninghe Damsté, J.S., 1996. Restricted utility of aryl isoprenoids as indicators for photic zone anoxia. Geochim. Cosmochim. Acta 60, 4873–4876.
Korn, D., 1991. Threedimensionally preserved clymeniids from the Hangenberg Black Shale of Drewer (Cephalopoda, Ammonoidea; Devonian/Carboniferous boundary, Rhenish Massif). Neues Jb. Geol. Paläontol. Monat. 119 (9), 553–563.
Korn, D., Weyer, D., 2003. High resolution stratigraphy of the Devonian-Carboniferous transitional beds in the Rhenish Mountains. Mitt. Mus. Naturkunde Berlin, Geowiss. Reihe 6, 79–124.
Krzemińska, E., Wiszniewska, J., Williams, I.S., 2006. Wczesnokarboński wiek intruzji platformowych w podłożu krystalicznym NE Polski. Prz. Geol. 54, 1093–1098.
Kumpan, T., Bábek, O., Kalvoda, J., Frýda, J., Matys Grygar, T., 2014a. A high-resolution, multiproxy stratigraphic analysis of the Devonian–Carboniferous boundary sections in the Moravian Karst (Czech Republic) and a correlation with the Carnic Alps (Austria). Geol. Mag. 151, 201–215.
Kumpan, T., Bábek, O., Kalvoda, J., Matys Grygar, T., Frýda, J., 2014b. Sea-level and environmental changes around the Devonian–Carboniferous boundary in the Namur–Dinant Basin (S Belgium, NE France): a multi-proxy stratigraphic analysis of carbonate ramp archives and its use in regional and interregional correlations. Sediment. Geol. 311, 43–59.
Kumpan, T., Bábek, O., Kalvoda, J., Matys Grygar, T., Frýda, J., Becker, R.T., Hartenfels, S., 2015. Petrophysical and geochemical signature of the Hangenberg Events: an integrated stratigraphy of the Devonian–Carboniferous boundary interval in the Northern Rhenish Massif (Avalonia, Germany). Bull. Geosci. 90, 667–694.
Lakin, J., Marshall, J., Troth, I., Harding, I., 2016. Greenhouse to icehouse: a biostratigraphic review of latest Devonian–Mississippian glaciations and their global effects. In: Becker, R.T., Königshof, P., Brett, C.E. (Eds.), Devonian Climate, Sea Level and Evolutionary Events. 423. Geological Society of London Special Publication, pp. 439–464.
Läufer, A.L., Hubich, D., Loeschke, J., 2001. Variscan geodynamic evolution of the Carnic Alps (Austria/Italy). Int. J. Earth Sci. Geol. Rundsch. 90, 855–870.
Lee, C.-T., Dee, S., 2019. Does volcanism cause warming or cooling? Geology 47, 687–688.
Lee, C.-T.A., Thurner, S., Paterson, S., Cao, W., 2015. The rise and fall of continental arcs: interplays between magmatism, uplift, weathering, and climate. Earth Planet. Sci. Lett. 425, 105–119.
Liermann, L.J., Mathur, R., Wasylenki, L.E., Nuester, J., Anbar, A.D., Brantley, S.L., 2011. Extent and isotopic composition of Fe and Mo release from two Pennsylvania shales in the presence of organic ligands and bacteria. Chem. Geol. 281, 167–180.
Lindström, S., Sanei, H., van de Schootbrugge, B., Pedersen, G.K., Lesher, C.E., Tegner, C., Heunisch, C., Dybkjær, K., Outridge, P.M., 2019. Volcanic mercury and mutagenesis in land plants during the end-Triassic mass extinction. Sci. Adv. 5, eaaw4018.
Liu, Y.-Q., Ji, Q., Kuang, H.-W., Jiang, X.-J., Xu, H., Peng, N., 2012. U–Pb zircon age, sedimentary facies, and sequence stratigraphy of the Devonian–Carboniferous boundary, Daposhang Section, Guizhou, China. Palaeoworld 21, 100–107.
Long, J.A., Large, R.R., Lee, M.S.Y., Benton, M.J., Danyushevsky, L.V., Chiappe, L.M., Halpin, J.A., Cantrill, D., Lottermoser, B., 2016. Severe selenium depletion in the Phanerozoic oceans as a factor in three global mass extinction events. Gondwana Res. 36, 209–218. https://doi.org/10.1016/j.gr.2015.10.001.
Lu, M., Lu, Y.H., Ikejiri, T., Hogancamp, N., Sun, Y., Wu, Q., Carroll, R., Çemen, I., Pashin, J., 2019. Forestation in the Southernmost Euramerica from Upper Devonian (Famennian) Black Shales. Sci. Rep. 9, 7581. https://doi.org/10.1038/s41598-019-43993-y 2.
Lundmark, A.M., Gabrielsen, R.H., Austrheim, H., Flaat, K., Strand, T., Ohm, S.E., 2012. Late Devonian rifting in the central North Sea: evidence from altered felsic volcanic rocks in the Embla oil field. Mar. Pet. Geol. 29, 204–218.
Mahoney, C., März, C., Buckman, J., Wagner, T., Blanco-Velandia, V.-O., 2019. Pyrite oxidation in shales: implications for palaeo-redox proxies based on geochemical and SEM-EDX evidence. Sediment. Geol. 389, 186–199.
Malec, J., 2014. The Devonian/Carboniferous boundary in the Holy Cross Mountains. Geol. Q. 58, 217–234.
Martinez, A., Boyer, D.L., Droser, M.L., Barrie, C., Love, G.D., 2019. A stable and productive marine microbial community was sustained through the end-Devonian Hangenberg Crisis within the Cleveland Shale of the Appalachian Basin, United States. Geobiology 17, 27–42.
Martínez Catalán, J.R., Fernández-Suárez, J., Meireles, C., González Clavijo, E., Belousova, E., Saeed, A., 2008. U–Pb detrital zircon ages in synorogenic deposits of the NW Iberian Massif (Variscan belt): interplay of Devonian–Carboniferous sedimentation and thrust tectonics. J. Geol. Soc. Lond. 165, 687–698.
Marynowski, L., Filipiak, P., 2007. Water column euxinia and wildfire evidence during deposition of the Upper Famennian Hangenberg event horizon from the Holy Cross Mountains (central Poland). Geol. Mag. 144, 569–595.
Marynowski, L., Kurkiewicz, S., Rakociński, M., Simoneit, B.R.T., 2011. Effects of weathering on organic matter: I. Changes in molecular composition of extractable organic compounds caused by paleoweathering of a Lower Carboniferous (Tournaisian) marine black shale. Chem. Geol. 285, 144–156.
Marynowski, L., Zatoń, M., Rakociński, M., Filipiak, P., Kurkiewicz, S., Pearce, T.J., 2012. Deciphering the upper Famennian Hangenberg Black Shale depositional environments based on multi-proxy record. Palaeogeogr. Palaeoclimatol. Palaeoecol. 346 (347), 66–86.
Marynowski, L., Pisarzowska, A., Rakociński, M., Derkowski, A., Środoń, J., Szaniawski, R., Cohen, A., 2017. Influence of palaeoweathering on trace metal concentrations and environmental proxies in black shales. Palaeogeogr. Palaeoclimatol. Palaeoecol. 472, 177–191.
Matsunaga, K., 1981. Oceanic residence time of mercury. Bull. Fac. Fish. Hokkaido Univ. 32 (2), 199–202.
Matyja, H., Sobień, K., Marynowski, L., Stepień-Sałek, M., Małkowski, K., 2015. The expression of the Hangenberg Event (latest Devonian) in arelatively shallow-marine succession (Pomeranian Basin, Poland):the results of a multi-proxy investigation. Geol. Mag. 152, 400–428.
Matyja, H., Woroncowa-Marcinowska, T., Filipiak, P., Brański, P., Sobień, K., 2020. The Devonian/Carboniferous boundary interval in Poland: multidisciplinary studies in pelagic (Holy Cross Mountainsand Sudetes) and ramp (Western Pomerania) successions. Palaeobiodivers. Palaeoenviron (in press).
McCann, T., Saintot, A., Chalot-Prat, F., Kitchka, A., Fokin, P., Alekseev, A., Europrobe-Intas Research Team, 2003. Evolution of the southern margin of the Donbass (Ukraine) from Devonian to Early Carboniferous times. In: McCann, T., Saintot, A. (Eds.), Tracing Tectonic Deformation Using the Sedimentary Record. Geol. Soc. London Spec. Publ. 208. pp. 117–135.
McCarty, D.K., Sakharov, B.A., Drits, V.A., 2009. New insights into smectite illitization: a zoned K-bentonite revisited. Am. Mineral. 94, 1653–1671.
McCarty, D.K., Theologou, P.N., Fischer, T.B., Derkowski, A., Stokes, M.R., Ollila, A., 2015. Mineral-chemistry quantification and petrophysical calibration for multi-mineral evaluations: a nonlinear approach. AAPG Bull. 99, 1371–1397.
McKenzie, N.R., Horton, B.K., Loomis, S.E., Stockli, D.F., Planavsky, N.J., Lee, C.-T.A., 2016. Continental arc volcanism as the principal driver of icehouse-greenhouse variability. Science 352, 444–447.
McKenzie, N.R., Horton, B.K., Loomis, S.E., Stockli, D.F., Planavsky, N.J., Lee, C.-T.A., 2016. Continental arc volcanism as the principal driver of icehouse-greenhouse variability. Science 352, 444–447.
Mouro, L.D., Rakociński, M., Marynowski, L., Pisarzowska, A., Musabelliu, S., Zatoń, M., Carvalho, M.A., Fernandes, A.C.S., Waichel, B.L., 2017. Benthic anoxia, intermittent photic zone euxinia and elevated productivity during deposition of the Lower Permian, post-glacial fossiliferous black shales of the Paraná Basin, Brazil. Glob. Planet. Chang. 158, 155–172.
Myrow, P.M., Hanson, A., Phelps, A.S., Creveling, J.R., Strauss, J.V., Fike, D.A., Ripperdan, R.L., 2013. Latest Devonian (Famennian) global events in western Laurentia: variations in the carbon isotopic record linked to diagenetic alteration below regionally extensive unconformities. Palaeogeogr. Palaeoclimatol. Palaeoecol. 386, 194–209.
Myrow, P.M., Ramezani, J., Hanson, A.E., Bowring, S.A., Racki, G., Rakociński, M., 2014. High-precision U–Pb age and duration of the latest Devonian (Famennian) Hangenberg event, and its implications. Terra Nova 26, 222–229.
Nägler, T.F., Siebert, C., Lüschen, H., Böttcher, M.E., 2005. Sedimentary Mo isotope record across the Holocene fresh-brackish water transition of the Black Sea. Chem. Geol. 219, 283–295.
Nägler, T.F., Neubert, N., Böttcher, M.E., Dellwig, O., Schnetger, B., 2011. Molybdenum isotope fractionation in pelagic euxinia: evidence from the modern Black and Baltic Seas. Chem. Geol. 289, 1–11.
Nakagawa, Y., Takano, S., Firdaus, M.L., Norisuye, K., Hirata, T., Vance, D., Sohrin, Y., 2012. The molybdenum isotopic composition of the modern ocean. Geochem. J. 46, 131–141.
Neubert, N., Nägler, T.F., Böttcher, M.E., 2008. Sulfidity controls molybdenum isotope fractionation into euxinic sediments: evidence from the modern Black Sea. Geology 36, 775–778.
Olempska, E., 1997. Changes in benthic ostracod assemblages across the Devonian–Carboniferous boundary in the Holy Cross Mountains. Poland. Acta Palaeontol. Pol. 42, 291–332.
Paproth, E., 1986. An introduction to a field trip to the Late Devonian outcrops in the northern Rhenishes Schiefergebirge (Federal Republic of Germany). Ann. Soc. Geol. Belg. 109, 275–284.
Paschall, O., Carmichael, S.K., Königshof, P., Waters, J.A., Ta, P.H., Komatsu, T., Dombrowski, A., 2019. The Devonian-Carboniferous boundary in Vietnam: sustained

ocean anoxia with a volcanic trigger for the Hangenberg Crisis? Glob. Planet. Chang. 175, 64–81.
Pasquarè Mariotto, F.P., Venturini, C., 2019. Birth and evolution of the Paleocarnic Chain in the Southern Alps: a review. Int. J. Earth Sci. https://doi.org/10.1007/s00531-019-01774-y.
Percival, L.M.E., Ruhl, M., Hesselbo, S.P., Jenkyns, H.C., Mather, T.M., Whiteside, J.H., 2017. Mercury evidence for pulsed volcanism during the end-Triassic mass extinction. Proc. Natl. Acad. Sci. U. S. A. 114 (30), 7929–7934. https://doi.org/10.1073/pnas.1705378114.
Payette, C., Martin, R.F., 1986. The harvey volcanic suite, New Brunswick. II. Postmagmatic adjustments in the mineralogy and bulk composition of a high-fluorine rhyolite. Can. Mineral. 24, 571–584.
Percival, L.M.E., Jenkyns, H.C., Mather, T.A., Dickson, A.J., Batenburg, S.J., Ruhl, M., Hesselbo, S.P., Barclay, R., Jarvis, I., Robinson, S.A., Woelders, L., 2018. Does large igneous province volcanism always perturb the mercury cycle? Comparing the records of Oceanic Anoxic Event 2 and the end-Cretaceous to other Mesozoic events. Am. J. Sci. 318, 799–860.
Percival, L.M.E., Selby, D., Bond, D.P.G., Rakociński, M., Racki, G., Adatte, T., Spangenberg, J.E., Föllmi, K.B., 2019. Osmium-isotope evidence for pulses of extreme continental weathering associated with multiple Late Devonian climate perturbations. Palaeogeogr. Palaeoclimatol. Palaeoecol. 524, 240–249.
Perri, M.C., Spalletta, C., 2001. Hangenberg Event al limite Devoniano/Carbonifero al Monte Zermula, Alpi Carniche, Italia. In: Perri, M.C. (Ed.), Giornate di Paleontologia 2001. 62 Giornale di Geologia, Ser. 3a Supplemento, 31-40.
Percival, L.M.E., Witt, M.L. I., Mather, T.A., Hermoso, M., Jenkyns, H.C., Hesselbo, S.P., Al-Suwaidi, A.H., Storm, M.S., Xu, W., Ruhl, M., 2015. Globally enhanced mercury deposition during the end-Pliensbachian extinction and Toarcian OAE: A link to the Karoo–Ferrar Large Igneous Province. Earth Planet. Sci. Lett. 428, 267–280.
Petrova, N.S., 2010. Pyroclastic rocks in deposits of the potassic subformation of the Pripyat intracontinental palaeorift. Geologia 36, 395–406.
Pouclet, A., El Hadi, H., Bardibtzeff, J.-M., Benharref, M., Fekkak, A., 2017. Devonian to Early Carboniferous magmatic alkaline activity in the Tafilalt Province, Eastearn Morocco: an Eovariscan episode in the Gondwana margin, north of the West African Craton. J. Afr. Earth Sci. 129, 814–841.
Pracht, M., 2000. Controls on magmatism in the Munster Basin, SW Ireland. In: Friend, P.F., Williams, B.P.J. (Eds.), New Perspectives on the OM Red Sandstone. Geological Society, London, Special Publications 180. pp. 303–317.
Pracht, M., Batchelor, R.A., 1998/99. A geochemical study of late Devonian and early Carboniferous tufts from the South Munster Basin, Ireland. Irish J. Earth Sci. 17 (25), 25–38.
Prestianni, C., Sautois, M., Denayer, J., 2016. Disrupted continental environments around the Devonian-Carboniferous Boundary: introduction of the tener event. Geol. Belg. 19 (1–2), 135–145.
Pujol, F., Berner, Z., Stüben, D., 2006. Palaeoenvironmental changes at the Frasnian/Famennian boundary in key European sections: chemostratigraphical constraints. Palaeogeogr. Palaeoclimatol. Palaeoecol. 240, 120–145.
Pyle, D.M., Mather, T.A., 2003. The importance of volcanic emissions for the global atmospheric mercury cycle. Atmos. Environ. 37, 5115–5124.
Qie, W., Liu, J., Chen, J., Wang, X., Mii, H.-S., Zhang, X., Huang, X., Yao, L., Algeo, T.J., Luo, G., 2015. Local overprints on the global carbonate δ13C signal in Devonian-Carboniferous boundary successions of South China. Palaeogeogr. Palaeoclimatol. Palaeoecol. 418, 290–303.
Racki, G., 2020a. A volcanic scenario for the Frasnian–Famennian major biotic crisis and other Late Devonian global changes: more answers than questions? Glob. Planet. Chang in press.
Racki, G., 2020b. Volcanism as a prime cause of mass extinction: retrospectives and perspectives. In: Adatte, T., Bond, D.P.G., Keller, G. (Eds.), Mass Extinctions, Volcanism, and Impacts: New Developments. Geological Society of America Special Paper 544https://doi.org/10.1130/2019.2544(01). in press.
Racki, G., Racka, M., Matyja, H., Devleeschouwer, X., 2002. The Frasnian/Famennian boundary interval in the South Polish-Moravian shelf basins: integrated event-stratigraphical approach. Palaeogeogr. Palaeoclimatol. Palaeoecol. 181, 251–297.
Racki, G., Marynowski, L., Rakociński, M., 2018a. Anomalous Upper Devonian mercury enrichments: comparison of Inductively Coupled Plasma – Mass Spectrometry (ICP-MS) and Atomic Absorption Spectrometry (AAS) analytical data. Geol. Q. 62, 487–495.
Racki, G., Rakociński, M., Marynowski, L., Wignall, P.B., 2018b. Mercury enrichments and the Frasnian-Famennian biotic crisis: a volcanic trigger proved? Geology 46, 543–546.
Rakociński, M., Zatoń, M., Marynowski, L., Gedl, P., Lehman, J., 2018. Redox conditions, productivity, and volcanic input during deposition of uppermost Jurassic and Lower Cretaceous organic-rich siltstones in Spitsbergen, Norway. Cretac. Res. 89, 126–147.
Rakociński, M., Marynowski, L., Pisarzowska, A., Bełdowski, J., Siedlewicz, G., Zatoń, M.M., Perri, M.C., Spalletta, C., Schönlaub, H.-P., 2020. Volcanic related methylmercury poisoning as the possible driver of the end-Devonian Mass Extinction. Sci. Rep (in press).
Ray, J.S., Pande, K., 1999. Carbonatite alkaline magmatism associated with continental flood basalts at stratigraphic boundaries: cause for mass extinctions. Geophys. Res. Lett. 26, 1917–1920.
Retallack, G.J., Huang, C., 2011. Ecology and evolution of Devonian trees in New York, USA. Palaeogeogr. Palaeoclimatol. Palaeoecol. 299, 110–128.
Ricci, J., Quidelleur, X., Pavlov, V., Orlov, S., Shatsillo, A., Courtillot, V., 2013. New 40Ar/39Ar and K–Ar ages of the Viluy traps (Eastern Siberia): further evidence for a relationship with the Frasnian–Famennian mass extinction. Palaeogeogr. Palaeoclimatol. Palaeoecol. 386, 531–540.
Richards, B.C., Higgins, A.C., 1988. Devonian–Carboniferous boundary beds of the Palliser and Exshaw Formations at Jura Creek, Rocky Mountains, Southwestern Alberta. In: McMillan, N.J., Embry, A.F., Glass, D.J. (Eds.), Devonian of the World. Canadian Society of Petroleum Geologists, Memoir 14. pp. 399–412.
Ridgwell, A.J., Kennedy, M.J., Caldeira, K., 2003. Carbonate deposition, climate stability, and Neoproterozoic ice ages. Science 302, 859–862.
Rimmer, S.M., 2004. Geochemical paleoredox indicators in Devonian-Mississippian black shales, Central Appalachian Basin (USA). Chem. Geol. 206, 373–391.
Rosa, D.R.N., Finch, A.A., Andersen, T., Inverno, C.M.C., 2008. U-Pb geochronology of felsic volcanic rocks hosted in the Gafo Formation, South Portuguese Zone: the relationship with Iberian Pyrite Belt magmatism. Mineral. Mag. 72, 1129–1144.
Rubin, K., 1997. Degassing of metals and metalloids from erupting seamount and mid-ocean ridge volcanoes: observations and predictions. Geochim. Cosmochim. Acta 61, 3525–3542. https://doi.org/10.1016/S0016 -7037(97)00179-8.
Sageman, B.B., Murphy, A.E., Werne, J.P., Ver Straeten, C.A., Hollander, D.J., Lyons, T.W., 2003. A tale of shales: the relative roles of production, decomposition, and dilution in the accumulation of organic-rich strata, Middle–Upper Devonian, Appalachian basin. Chem. Geol. 195, 229–273.
Sallan, L.C., Coates, M.I., 2010. End-Devonian extinction and a bottleneck in the early evolution of modern jawed vertebrates. Proc. Natl. Acad. Sci. 107, 10131–10135.
Sandberg, C.A., Morrow, J.R., Ziegler, W., 2002. Late Devonian sea-level changes, catastrophic events, and mass extinctions. Geol. Soc. Am. Spec. Pap. 356, 473–487.
Sanei, H., Grasby, S., Beauchamp, B., 2012. Latest Permian mercury anomalies. Geology 40, 63–66.
Sarmiento, J.L., Gruber, N., 2006. Ocean Biogeochemical Dynamics. Princeton university press, New Jersey, USA 503 pp.
Schobben, M., van de Schootbrugge, B., Wignall, P., 2019. Interpreting the carbon isotope record of mass extinctions. Elements 15, 331–337.
Schönlaub, H.P., Histon, K., 2000. The Paleozoic evolution of the southern Alps. Mitt. Österr. Geol. Gessel. 92, 15–34.
Schönlaub, H.-P., 2018. Review of the Devonian/Carboniferous boundary in the Carnic Alps. Jb. Geol. B.-A 158 (1-4), 29–47.
Schönlaub, H.P., Attrep, M., Boeckelmann, K., Dreesen, R., Feist, R., Fenninger, A., Hahn, G., Klein, P., Korn, D., Kratz, R., Magaritz, M., Orth, C.J., Schramm, J.-M., 1992. The Devonian/Carboniferous Boundary in the Carnic Alps (Austria) – a multidisciplinary approach. Jb. Geol. Bundesanst. 135, 57–98.
Scott, C., Lyons, T.W., 2012. Contrasting molybdenum cycling and isotopic properties in euxinic versus non-euxinic sediments and sedimentary rocks: refining the paleoproxies. Chem. Geol. 324-325, 19–27.
Sengör, A.M.C., Atayman, S., 2009. The Permian extinction and the Tethys: an exercise in global geology. In: Geological Society of America Speical Paper. 448 Colorado, Boulder.
Shaw, T.J., Gieskes, J.M., Jahnke, R.A., 1990. Early diagenesis in differing depositional environments: the response of transition metals in pore water. Geochim. Cosmochim. Acta 54, 1233–1246.
Shizuya, A., Oba, M., Ando, T., Ogata, Y., Takashima, R., Nishi, H., Komatsu, T., Nguyen, P.D., 2020. Variations in trace elements, isotopes, and organic geochemistry during the Hangenberg Crisis, Devonian–Carboniferous transition, northeastern Vietnam. Island Arc 29, e12337.
Siebert, C., Nägler, T.F., Kramers, J.D., 2001. Determination of molybdenum isotope fractionation by double-spike multicollector inductively coupled plasma mass spectrometry. Geochem. Geophys. Geosyst. 2 2000GC000124.
Siebert, C., Nägler, T.F., von Blanckenburg, F., Kramers, J.D., 2003. Molybdenum isotope record as a potential new proxy for paleoceanography. Earth Planet. Sci. Lett. 211, 159–171.
Siebert, C., McManus, J., Bice, A., Poulson, R., Berelson, W.M., 2006. Molybdenum isotope signatures in continental margin marine sediments. Earth Planet. Sci. Lett. 241, 723–733.
Simon, L., Goddéris, Y., Buggisch, W., Strauss, H., Joachimski, M.M., 2007. Modeling the carbon and sulfur isotope compositions of marine sediments: climate evolution during the Devonian. Chem. Geol. 246, 19–38.
Sinninghe Damsté, J.S., Schouten, S., 2005. Biological markers for anoxia in the photic zone of the water column. Handb. Environ. Chem. 2, 1–37.
Spalletta, C., Perri, M.C., Pondrelli, M., Corradini, C., Mossoni, A., Schönlaub, H.P., 2015. Pal grande formation. In: Corradini, C., Suttner, T.J. (Eds.), The Pre-Variscan sequence of the Carnic Alps (Austria and Italy). Abhandlungen der Geologischen Bundesanstalt 69. pp. 137–140.
Spalletta, C., Corradini, C., Feist, R., Korn, D., Kumpan, T., Perri, M.C., Peondrelli, M., Venturini, C., 2020. The Devonian–Carboniferous Boundary in the Carnic Alps (Austria and Italy). Palaeobiodivers. Palaeoenviron. https://doi.org/10.1007/s12549-019-00413-3.
Spalletta, C., Perri, M.C., Over, D.J., Corradini, C., 2017. Famennian (Upper Devonian) conodont zonation: revised global standard. Bull. Geosci. 92 (1), 31–57. https://doi.org/10.1340/bull.geosci.1623.
Spalletta, C., Venturini, C., 1995. Late Devonian-Early Carboniferous synsedimentary tectonic evolution of the Palaeocarnic domain (Southern Alps, Italy). Giornale di Geologia 56 2 (1994), 211–222.
Streel, M., Caputo, M.V., Loboziak, S., Melo, J.H.G., 2000. Late Frasnian–Famennian climates based on palynomorph analyses and the question of the Late Devonian glaciations. Earth Sci. Rev. 52, 121–173.
Stricanne, L., Munnecke, A., Pross, J., 2006. Assessing mechanisms of environmental change: palynological signals across the late Ludlow (Silurian) positive isotope excursion (δ13C, δ18O) on Gotland, Sweden. Palaeogeogr. Palaeoclimatol. Palaeoecol. 230, 1–31.
Svensen, H.H., Torsvik, T., Callegaro, S., Augland, L., Heimdal, T.H., Jerram, D.A., Planke, S., Pereira, E., 2018. Gondwana Large Igneous Provinces: plate reconstructions, volcanic basins and sill volumes. In: Sensarma, S., Storey, B. (Eds.), Large

Igneous Provinces from Gondwana and Adjacent Regions. Geological Society Special Publication 463. pp. 17–40.
Tabor, C.R., Bardeen, C.G., Otto-Bliesner, B.L., Garcia, R.R., Toon, O.B., 2020. Causes and climatic consequences of the impact winter at the Cretaceous-Paleogene boundary. Geophys. Res. Lett. 47, e60121.
Takahashi, S., Kaiho, K., Oba, M., Kakegawa, T., 2010. A smooth negative shift of organic-carbon isotope ratios at an end-Permian mass extinction horizon in central pelagic Panthalassa. Palaeogeogr. Palaeoclimatol. Palaeoecol. 292, 532–539.
Taylor, S.R., McLennan, S.M., 1985. The Continental Crust: Its Composition and Evolution. Blackwell, Oxford, pp. 312.
Trapp, E., Kaufmann, B., Mezger, K., Korn, D., Weyer, D., 2004. Numerical calibration of the Devonian-Carboniferous boundary: two new U-Pb isotope dilution–thermal ionization mass spectrometry single-zircon ages from Hasselbachtal (Sauerland, Germany). Geology 32, 857–860.
Tribovillard, N., Algeo, T.J., Lyons, T., Riboulleau, A., 2006. Trace metals as paleoredox and paleoproductivity proxies: an update. Chem. Geol. 232, 12–32.
Tribovillard, N., Algeo, T.J., Baudin, F., Riboulleau, A., 2012. Analysis of marine environmental conditions based on molybdenum–uranium covariation – applications to Mesozoic paleoceanography. Chem. Geol. 324–325, 46–58.
Tucker, R.D., Bradley, D.C., Ver Straeten, C.A., Harris, A.G., Ebert, J.R., McCutcheon, S.R., 1998. New U-Pb zircon ages and the duration and division of Devonian time. Earth Planet. Sci. Lett. 158, 175–186.
Turgeon, S., Brumsack, H.-J., 2006. Anoxic vs dysoxic events reflected in sediment geochemistry during the Cenomanian–Turonian Boundary Event (Cretaceous) in the Umbria–Marche Basin of central Italy. Chem. Geol. 234, 321–339.
Uveges, B.T., Junium, C.K., Boyer, D.L., Cohen, P.A., Day, J.E., 2018. Biogeochemical controls on black shale deposition during the Frasnian-Famennian biotic crisis in the Illinois and Appalachian Basins, USA, inferred from stable isotopes of nitrogen and carbon. Palaeogeogr. Palaeoclimatol. Palaeoecol. https://doi.org/10.1016/j.palaeo.2018.05.031.
Van Steenwinkel, M., 1984. Sedimentology of the Devonian-Carboniferous boundary sediments in the Oberrödinghausen 1 borehole (Germany). Cour. Forschungsinstitut Senckenb. 67, 123–137.
Van Steenwinkel, M., 1993. The D/C boundary: comparison between the Dinant synclinorium and the northern border of the Rhenish Slate Mountains, a sequence-stratigraphic view. Ann. Soc. Geol. Belg. 115, 665–681.
Venturini, C., Spalletta, C., 2015. Dimon formation. In: Corradini, C., Suttner, T.J. (Eds.), The Pre-Variscan sequence of the Carnic Alps (Austria and Italy). 69. Abhandlungen der Geologischen Bundesanstalt, Wien, pp. 155–158.
Ver Straeten, C.A., Brett, C.E., Sageman, B.B., 2011. Mudrock sequence stratigraphy: a multi-proxy (sedimentological, paleobiological and geochemical) approach, Devonian Appalachian Basin. Palaeogeogr. Palaeoclimatol. Palaeoecol. 304, 54–73.
Wainwright, A.J., Tosdal, R.M., Forster, C.N., Kirwin, D.J., Lewis, P.D., Wooden, J.L., 2011. Devonian and Carboniferous arcs of the Oyu Tolgoi porphyry Cu-Au district, South Gobi region, Mongolia. Geol. Soc. Am. Bull. 123, 306–328.
Wall-Palmer, D., Jones, M.T., Hart, Mb, Fisher, J.K., Smart, C.W., Hembury, D.J., Palmer, M.R., Fones, G.R., 2011. Explosive volcanism as a cause for mass mortality of pteropods. Mar. Geol. 282, 231–239.
Ward, W., Strauss, J.V., Johnson, B.G., McClelland, W.C., Colpron, M., von Gosen, W., Piepjohn, K., Cobble, M., Crockford, P.W., Landis, J., 2019. Age, geochemistry and significance of Devonian felsic magmatism in the North Slope subterrane, Yukon. In: Piepjohn, K., McClelland, W.C., Strauss, J.V., Reinhart, L. (Eds.), Circum-Arctic Structural Events: Tectonic Evolution of the Arctic Margins and Trans-Arctic Links with Adjacent Orogens. Geological Society of America, Special Paper 541.
Wedepohl, K.H., 1970. Geochemische Daten von sedimentären Karbonaten und Karbonatgesteinen in ihrem faziellen und petrogenetischen Aussgewert. Verh. Geol. Bundesanst. 4, 692–705.
Weissert, H., Erba, E., 2004. Volcanism, CO2 and palaeoclimate: a Late Jurassic-Early Cretaceous carbon and oxygen isotope record. J. Geol. Soc. 161 (4), 695–702.
Wignall, P.B., 2005. The link between large igneous province eruptions and mass extinctions. Elements 1, 293–297.
Wignall, P., Newton, R., 1998. Pyrite framboid diameter as a measure of oxygen deficiency in ancient mudrocks. Am. J. Sci. 298, 537–552.
Wilder, H., 1994. Death of Devonian reefs – implications and further investigations. Cour. Forsch.-Inst. Senckenb. 172, 241–247.
Wilson, M., Lyashkevlch, Z.M., 1996. Magmatism and the geodynamics of rifting of the Pripyat-Dnieper-Donets rift, East European Platform. Tectonophysics 268, 65–81.
Winter, J., 2015. Vulkanismus und Kellwasser-Krise – Zirkon-Tephrostratigrafie, Identifizierung und Herkunft distaler Fallout-Aschenlagen (Oberdevon, Synklinorium von Dinant, Rheinisches Schiefergebirge, Harz). Z. Dt. Ges. Geowiss. 166, 227–251.
Woroncowa-Marcinowska, T., 2017. Latest Devonian silicified agglutinated foraminifera near the Hangenberg event horizon from Kowala (Holy Cross Mountains) and Wapnica Quarries (Sudetes), Poland. In: Kaminski, M.A., Alegret, L. (Eds.), Proceedings of the Ninth International Workshop on Agglutinated Foraminifera. Grzybowski Foundation Special Publication 22. pp. 251–261.
Yang, S., 2019. Reconstruction of Local and Global Marine Paleoredox Conditions during Deposition of the Devonian-Mississippian Exshaw Formation (Black Shale Member) and the Evaluation of Hydrocarbon Maturation Effects. unpublished Master Thesis. University of Waterloo, Ontario, Canada.
Young, A., Flament, N., Maloney, K., Williams, S., Matthews, K., Zahirovic, S., Dietmar Müller, R., 2019. Global kinematics of tectonic plates and subduction zones since the late Paleozoic Era. Geosci. Front. 10, 989–1013.
Zerkle, A.L., Scheiderich, K., Maresca, J.A., Liermann, L.J., Brantley, S.L., 2011. Molybdenum isotope fractionation by cyanobacterial assimilation during nitrate utilization and N_2 fixation. Geobiology 9, 94–106.
Zhuravlev, A.V., Sobolev, D.B., 2019. Devonian-Carboniferous boundary in the East of the Pechora Plate (Kamenka River and Vangyr River sections). Vestnik IG Komi SC UB RAS 10, 16–22. https://doi.org/10.19110/2221-1381-2019-10-16-22.
Ziegler, P.A., 1990. Geological Atlas of Western and Central Europe, Second ed. Shell International Petroleum, Maatschappij B.V.